Residual stress-constrained space–time topology optimization for multi-axis additive manufacturing

Wu, Kai; van Keulen, Fred; Wu, Jun

DOI
10.1016/j.cma.2025.117913

Publication date
2025

Document Version
Final published version

Published in
Computer Methods in Applied Mechanics and Engineering

Computer Methods in Applied Mechanics and Engineering 440 (2025) 117913

Contents lists available at ScienceDirect

Comput. Methods Appl. Mech. Engrg.

journal homepage: www.elsevier.com/locate/cma

Residual stress-constrained space–time topology optimization for multi-axis additive manufacturing

Kai Wu [a], Fred van Keulen [a], Jun Wu [b,*]

[a] Faculty of Mechanical Engineering, Delft University of Technology, Mekelweg 2, Delft, 2628 CD, The Netherlands
[b] Faculty of Industrial Design Engineering, Delft University of Technology, Landbergstraat 15, Delft, 2628 CE, The Netherlands

GRAPHICAL ABSTRACT

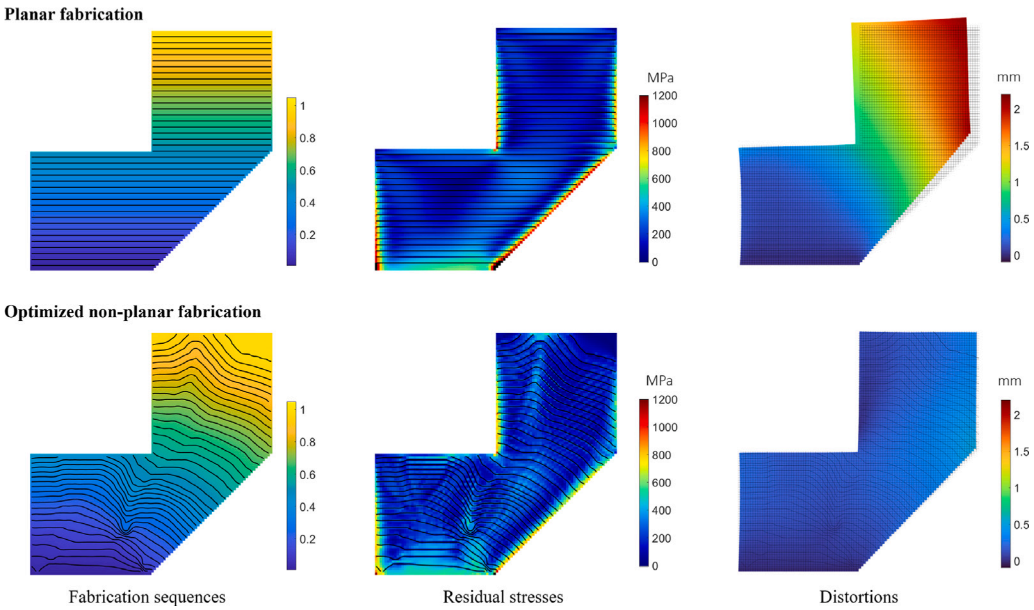

ARTICLE INFO

Keywords:
Multi-axis additive manufacturing
Wire arc additive manufacturing
Fabrication sequence optimization
Topology optimization

ABSTRACT

Residual stresses and distortions are major barriers to the broader adoption of wire arc additive manufacturing. These issues are coupled and arise due to large thermal gradients and phase transformations during the directed energy deposition process. Mitigating distortions may lead to substantial residual stresses, causing cracks in the fabricated components. In this paper, we propose a novel method to reduce both residual stresses and distortions by optimizing

* Corresponding author.
E-mail address: j.wu-1@tudelft.nl (J. Wu).

https://doi.org/10.1016/j.cma.2025.117913
Received 23 October 2024; Received in revised form 3 February 2025; Accepted 5 March 2025

Available online 21 March 2025
0045-7825/

Residual stress

the fabrication sequence. This approach explores the use of non-planar layers, leveraging the increased manufacturing flexibility provided by robotic arms. Additionally, our method allows for the concurrent optimization of the structural layout and corresponding fabrication sequence. We employ the inherent strain method as a simplified process simulation model to predict residual stresses and distortions. Local residual stresses are aggregated using a p-norm function, which is integrated into distortion minimization as a constraint. Through numerical examples, we demonstrate that the optimized non-planar fabrication strategies can effectively reduce both residual stresses and distortions.

1. Introduction

Additive manufacturing has advanced rapidly in the past two decades. An important recent advancement is the introduction of robotic arms for 3D printing, which enables the production of large parts. In contrast to a fixed build orientation in Cartesian-type 3D printing, robotic arms provide rotational motion, further increasing manufacturing flexibility. By continuously adjusting the build orientation, robotic systems enable the deposition of material along non-planar layers, offering the possibility to avoid supports and improve manufacturing quality. These robotic systems have been employed for printing with both polymers and metals—using material extrusion for polymers [1,2] and directed energy deposition techniques like wire arc additive manufacturing (WAAM) for metals [3–5]. WAAM, also known as wire arc directed energy deposition (WA-DED) [6,7], combines traditional welding methods with modern additive manufacturing principles. It typically uses an electric arc as the heat source to melt a metal wire and deposit it layer by layer to build 3D components. It offers a cost-effective and efficient solution for producing large, customized metal parts, often with complex geometries that are impractical to achieve with conventional manufacturing.

However, the adoption of WAAM in critical industries is hindered by several challenges, particularly residual stresses and distortions [8–10]. As a directed energy deposition process, WAAM involves high energy input, large thermal gradients, multiple phase transformations, and repeated heating and cooling cycles. These factors result in significant residual stresses and distortions in the fabricated components. The residual stresses can lead to cracking [11] and large deflections during fabrication as well as upon unclamping [12]. Consequently, residual stresses compromise the reliability of the parts, while distortions often render them unusable without extensive and costly post-processing.

From a manufacturing perspective, various strategies have been employed to mitigate residual stresses. These include adjusting process parameters such as scanning speed, cooling rate, and welding mode [13], as well as implementing in situ temperature control to reduce temperature gradients [12]. Additionally, post-process treatments such as annealing and rolling [14–17] are also commonly used. However, these measures often require significant upgrades to the entire system, which can be impractical due to the large scale of the parts and the constraints of existing manufacturing setups.

Residual stresses are closely related to the structural design. Design guidelines to avoid excessive distortions and residual stresses have been proposed for relatively simple geometries [5,18,19]. For complex continuum structures, structural optimization has been pursued to address these issues, primarily for Cartesian-type 3D printing based on powder beds. Allaire and Jakabčin [20] proposed a thermo-elastic model to predict the accumulation of residual stress and distortion, and integrated it into shape and topology optimization. Similarly, Misiun et al. [21] minimized thermal-induced distortion through structural optimization to avoid recoater collisions and build failures, adopting an inherent strain method for process simulation. Furthermore, Xu et al. [22] included constraints on residual stresses in topology optimization. Besides structural optimization, residual stresses can be mitigated through support structure optimization [23–25]. Bruggi et al. [26] concurrently optimized the structural layout and constant build orientation to design lightweight structures, accounting for the material anisotropy in WAAM [27–29].

In this paper, we propose optimizing the fabrication sequence to mitigate residual stresses and distortions in multi-axis additive manufacturing. In traditional Cartesian-based 3D printing, the layers are planar, and they are determined by a fixed build orientation. In multi-axis additive manufacturing, however, the rotational motion allows to deposit material along curved layers. By fabrication sequence in multi-axis additive manufacturing, we refer to a decomposition of the component into curved layers with varying orientations that are fabricated one upon another. It thus can be viewed as curved slicing, which, however, has been typically treated as a geometric problem, focusing on generating smoothly varying layers that the robotic arms can execute without collisions [1,30–32]. In curved slicing, the material anisotropy due to curved layers has been taken into account [33]. However, the critical impact of curved fabrication sequences on residual stresses is an open research question, with optimization largely unexplored. This challenge requires simulating the additive manufacturing process and its underlying physics. Research from the related field of robotic welding has shown that the joining sequence significantly impacts residual stresses and distortions [34,35]. Building on these insights, Wang et al. [36] demonstrated numerically that fabrication sequence optimization provides a viable and effective way to minimize thermally induced distortions. However, the reduction of distortions may be accompanied by increased residual stresses, making it a critical next step to limit residual stresses in fabrication sequence optimization.

While the fabrication sequence for residual stresses in the context of multi-axis printing has not been studied, it is worth mentioning a few papers that deal with scanning path optimization in Cartesian-based 3D printing. Chen et al. [37] proposed a scanning path optimization method based on level-set functions. The material anisotropy from the 2D scanning path is explored to reduce residual stresses. Boissier et al. [38] proposed scanning path optimization based on shape optimization theory, incorporating the simulation of the manufacturing process to minimize overheating and thus avoid excessive thermally induced residual stresses. This was later integrated with structural optimization to concurrently optimize the shape and the 2D scanning path [39].

Our method for reducing residual stresses and thermal-induced distortions is based on space–time topology optimization [40,41]. Its core idea is to represent curved layers using isolines of a scalar field. This scalar field, which is optimized in an iterative process, defines the pseudo-time at which each spatial point is materialized. From the pseudo-time field, a series of intermediate structures can be derived, representing the additive fabrication process. This optimization centers on analyzing residual stresses and distortions arising from the intermediate structures. This pseudo-time field can also be optimized concurrently with the structural layout, represented by a pseudo-density field as in conventional density-based topology optimization. In this concurrent optimization, in addition to residual stresses and distortions, the structural performance (e.g., compliance) is also taken into account.

A key element in the optimization is to predict residual stresses efficiently. The inherent strain method has gained popularity as a simplified process model to predict distortions and residual stresses [42–46]. The inherent strain method simplifies the complex thermo-mechanical interactions as an inelastic inherent strain field, which can be calibrated from experimental tests. It is an attractive alternative to high-fidelity methods for its computational efficiency. This is particularly useful for optimization problems that require repeated process simulations. For simplicity, in this research, we assume that the inherent strain field is homogeneous and isotropic and its value does not change with respect to different fabrication sequences. These assumptions serve the purpose of demonstrating the effectiveness of the presented workflow. We expect more accurate process models [47–50] can be integrated as well, albeit with the trade-off of more demanding computation. After obtaining the accumulation of residual stress layer by layer from the inherent strain method, we formulate the residual stresses as a constraint function in the optimization framework.

To incorporate residual stresses into optimization, we refer to general approaches dealing with stress constraints in topology optimization. Topology optimization with stress constraints has been extensively studied over the past decades, leading to the development of effective solutions for overcoming key challenges. The first challenge is the local nature of stress, resulting in a large number of constraints. A typical approach to managing a large number of local constraints is to aggregate them into a single global constraint using either p-norm or p-mean [51] or Kreisselmeier–Steinhauser function [52]. An alternative to this is based on augmented Lagrangian formulations [53,54], which transform the original constrained optimization problem into a sequence of unconstrained subproblems. The second challenge is the 'singularity' problem: the feasible solution space of a stress-constrained problem contains degenerate subspaces with a lower dimension. This makes it difficult to find the global optimum using gradient-based algorithms. Relaxation of the stress constraints using ϵ-relaxation [55] or qp-approach [56,57] has proven effective in alleviating this problem. In addition, Verbart et al. [58] has demonstrated that aggregating the local constraints using a lower bound aggregation function also effectively relaxes the feasible space. In this research, we build on these established methods for dealing with the local residual stresses. Specifically, local residual stresses are relaxed using the qp-approach and then aggregated into a global constraint using the p-norm function.

The remainder of the paper is organized as follows. Section 2 elaborates the mathematical model of the proposed method in detail. Section 3 validates the effectiveness of the proposed method with a series of numerical examples. Lastly, Section 4 summarizes the key findings and conclusions.

2. Methodology

In the methodology section, we first introduce the basis of space–time topology optimization, where the fabrication sequence is optimized, optionally together with the structural layout. We then present the evaluation of residual stresses and distortions in additive manufacturing, using an inherent strain method. Building on these key ingredients, we formulate a constraint function to restrict the maximum residual stress. Finally, we elaborate on the formulation of space–time topology optimization incorporating the residual stress constraint.

2.1. Space–time parameterization

In space–time topology optimization, the 3D printing sequence for fabricating a component is optimized simultaneously with the component's structural design. The fabrication sequence is represented by a scalar field, referred to as the pseudo-time field (or simply time field), which is defined over a finite element discretization of the component. This element-wise representation is analogous to density-based topology optimization, where each element is assigned a pseudo-density value. However, unlike the ideal binary density values ($\rho_e \in \{0, 1\}$) that indicate whether an element is solid or void, the time field is continuous ($t_e \in [0.0, 1.0]$), with smaller time values corresponding to elements materializing earlier in the manufacturing process.

From the density and time fields, one can derive a series of intermediate structures during fabrication. This is essential for simulating the additive manufacturing process and the physics involved in fabrication. Fig. 1 illustrates the calculation of intermediate structures. Fig. 1(a) shows the density field, representing the structural design of a component, while Fig. 1(d) illustrates a continuous time field, whose isolines represent the fabrication sequence. An intermediate structure from this fabrication sequence is shown in Fig. 1(e). Fig. 1(b)–(c) represent intermediate steps for computing the time field, and will be explained shortly. At a time point τ, elements with time values smaller than τ have been fabricated, while elements with time values larger than τ have not. The intermediate structure at time point τ, denoted by $\rho^{\{\tau\}}$, thus consists of

$$\rho_e^{\{\tau\}} = \begin{cases} \rho_e, & \text{if } t_e \le \tau, \\ 0, & \text{otherwise.} \end{cases} \tag{1}$$

To facilitate gradient-based optimization, this conditional equation is replaced by an element-wise multiplication of the density field and a modified time field,

$$\rho_e^{\{\tau\}} = \rho_e \bar{t}_e^{\{\tau\}}. \tag{2}$$

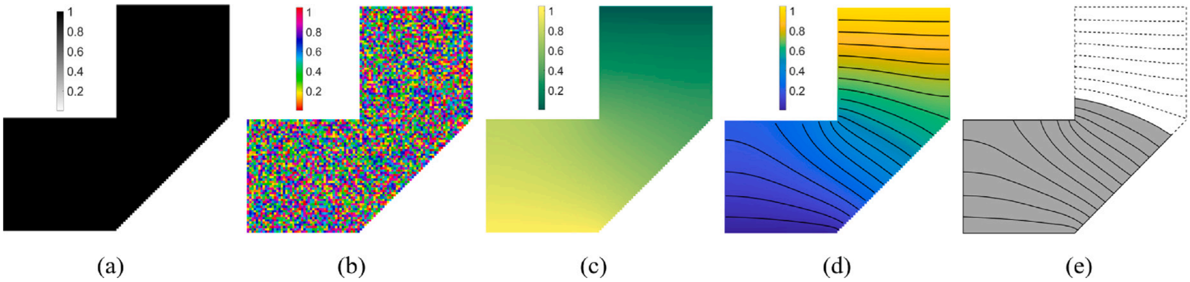

Fig. 1. Illustration of representations in space–time topology optimization. (a) The structural layout, represented by a density field $\boldsymbol{\rho}$. (b) A pseudo thermal diffusivity field, serving as optimization variables. For illustration purposes only, a random thermal diffusivity field is shown here. (c) The temperature field $\boldsymbol{T}$ obtained by solving the heat equation. (d) The time field $\boldsymbol{t}$ obtained from the temperature field using $\boldsymbol{t} = \mathbf{1} - \boldsymbol{T}$. Its isolines partition the component into 20 layers. (e) The 12-th intermediate structure during the manufacturing process, i.e., 12 layers have been manufactured and 8 layers are yet to be manufactured.

Specifically, the time field is modified by converting time values smaller than the threshold value τ to 1, and conversely, time values larger than τ to 0. This is implemented using a smoothed Heaviside function,

$$\bar{t}_e^{\{\tau\}} = 1 - \frac{\tanh(\beta_t \tau) + \tanh(\beta_t (t_e - \tau))}{\tanh(\beta_t \tau) + \tanh(\beta_t (1 - \tau))}, \tag{3}$$

where β_t determines the sharpness of the step function. A continuation scheme is applied to β_t during optimization. It starts with a low value for reduced nonlinearity and gradually increases to achieve distinct layer segmentation by the end of the optimization process. Later in the results section, we compare simulation results using the differential formulation (Eq. (2)) and binary classification (Eq. (1)).

To simulate the additive manufacturing process, a series of intermediate structures is computed. Let the fabrication of the component consist of N layers, where N is specified by the user. The component is divided by time points that are evenly spaced over the interval $[0, 1]$, $\tau_j = \frac{j}{N}$, where $j = 0, 1, \ldots, N$. We use $\boldsymbol{\rho}^{\{j\}}$ to indicate the j-th intermediate structure, i.e., corresponding to the time point τ_j. For example, the intermediate structure shown in Fig. 1(e) is $\boldsymbol{\rho}^{\{12\}}$, where the total number of layers is $N = 20$. The intermediate structure $\boldsymbol{\rho}^{\{j\}}$ for $j = 1, \ldots, N-1$ is calculated using Eq. (2), while $\boldsymbol{\rho}^{\{0\}} = \mathbf{0}$, and $\boldsymbol{\rho}^{\{N\}} = \boldsymbol{\rho}$.

It is worth noting that instead of directly optimizing the time field and thus the fabrication sequence, it is solved through a partial differential equation (PDE), where the coefficients in the equation are optimization variables [41]. This approach avoids discontinuities in the time field that could arise from direct optimization. Specifically, this PDE describes the heat diffusion from the baseplate where the fabrication starts. The element-wise thermal diffusivity (μ) determines the temperature distribution (T),

$$\nabla(\boldsymbol{\rho}\boldsymbol{\mu}\nabla\boldsymbol{T}) - \alpha_{\mathrm{T}}\boldsymbol{T} = 0. \tag{4}$$

Here ∇ is the vector differential operator. α_{T} denotes a constant drain rate. The boundary of the component adjacent to the baseplate is set as the heat source with a constant temperature of $T = 1$, while the other boundaries of the component are insulted. This heat equation is introduced to obtain a scalar field that monotonically varies from the baseplate toward the distant boundary of the component. It should not be confused with the thermal process in metal additive manufacturing. The heat equation takes into account the evolving structural layout during iterative optimization by including the density field $\boldsymbol{\rho}$. The optimization variables $\boldsymbol{\mu}$ are restricted between 0 and 1. The constant drain term is selected such that the temperature field smoothly varies from 1 to 0. After solving the heat equation, the temperature field is transformed by

$$\boldsymbol{t} = \mathbf{1} - \boldsymbol{T} \tag{5}$$

to obtain a pseudo-time field $\boldsymbol{t}$. By this transformation, elements adjacent to the baseplate, with a constant temperature of $T = 1$, are assigned $t = 0$, correctly serving as the starting point of fabrication.

2.2. Residual stresses calculation using the inherent strain method

The inherent strain method is a computationally efficient approach to predict deformations and residual stresses in metal components produced by additive manufacturing. It simplifies the complex thermal–mechanical phenomena in additive manufacturing by decoupling the thermal and mechanical problems, focusing on deformation without performing a full thermal analysis. For computational efficiency, the inherent strain method is often applied layer by layer by assigning inherent strain values to each newly deposited layer, and predicting the deformation of the component due to the equivalent mechanical load acting on this layer.

In this study, we adopt the assumptions of geometric and material linearity to ensure computational efficiency in calculating the mechanical response. While nonlinear analysis could improve simulation accuracy under significant residual stresses and distortions, we find it computationally prohibitive for optimization purposes. The premise of our approach is that by optimization we will reduce residual stresses and distortions to a level where linearity assumptions remain valid. As pointed out by Munro et al. [45], under the

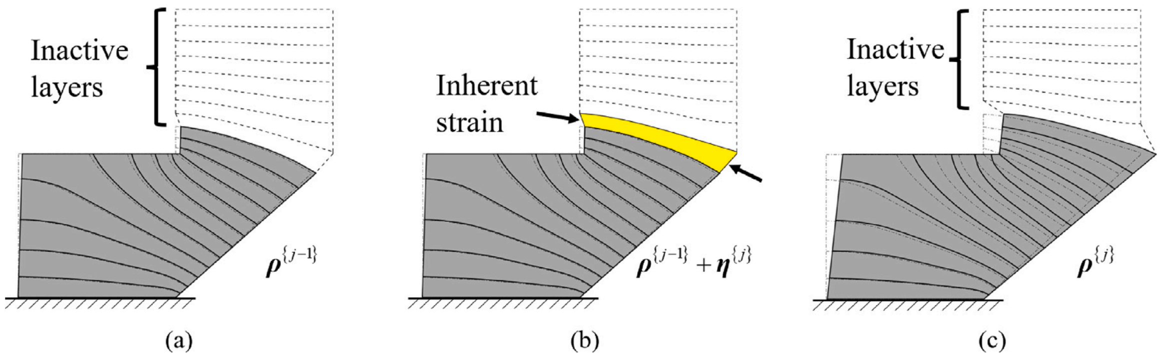

Fig. 2. Illustration of the inherent strain method in space–time topology optimization. (a) The 12-th intermediate structure, with deformation resulting from manufacturing the first 12 layers. (b) When the 13-th layer is deposited, the inherent strain field on this new layer is activated from its stress-free state. (c) The activation of the strain field on this new layer results in further deformation of the current intermediate structure. The inactive layers that have not been manufactured yet stay undeformed.

linearity assumptions, the total deformations and residual stresses of the entire component are the superposition of all increments due to the deposition of each layer.

$$\mathbf{U}_{\text{thermal}} = \sum_j \Delta \mathbf{U}^{\{j\}}, \tag{6}$$

$$\boldsymbol{\sigma} = \sum_j \Delta \boldsymbol{\sigma}^{\{j\}}. \tag{7}$$

Here the superscript $\{j\}$ indicates the increment in the displacement or residual stress due to the deposition of the j-th layer. We explain the calculation of the increments in the following.

In space–time topology optimization, a newly added layer is identified by the difference between two consecutive intermediate structures,

$$\boldsymbol{\eta}^{\{j\}} = \boldsymbol{\rho}^{\{j\}} - \boldsymbol{\rho}^{\{j-1\}},\ j = 1, 2, \ldots, N. \tag{8}$$

By activating the inherent strain in each new layer, the incremental deformation and residual stress on the intermediate structure can be calculated. This is illustrated in Fig. 2. Fig. 2(a) shows an intermediate structure $\rho^{\{j-1\}}$, with $j-1$ layers already manufactured. The intermediate structure is already deformed due to previous manufacturing steps. Fig. 2(b) highlights the deposition of a new layer. The inherent strain of this new layer is then activated, creating equivalent nodal forces on each element within this new layer,

$$\mathbf{F}_e = \int_{\Omega_e} \mathbf{B}^\top \mathbf{D} \boldsymbol{\varepsilon}^* d\Omega_e, \tag{9}$$

where $\mathbf{B}$ is the strain–displacement matrix, $\mathbf{D}$ is the constitutive matrix, $\boldsymbol{\varepsilon}^*$ is the inherent strain vector. In this study, we use an isotropic inherent strain to simplify the analysis by disregarding directional effects resulting from fabrication sequences. This approach ensures that the inherent strain field is independent of fabrication sequences, providing a consistent basis for comparing the effects of different sequences. While anisotropic inherent strain could be integrated into the framework – by deriving local material deposition orientation from the gradient of the time field – we focus on the role of fabrication sequence in this work, leaving the exploration of anisotropic effects as a natural extension for future studies.

The nodal forces on each element are then assembled to obtain a global force vector for the entire component,

$$\mathbf{F}^{\{j\}} = \sum_e \eta_e^{\{j\}^\kappa} \mathbf{F}_e, \tag{10}$$

where $\sum_e$ represents the assembly over all elements. Note that the forces are scaled by a factor that depends on the new layer $\boldsymbol{\eta}$. This is because in space–time topology optimization, the structural layout, represented by the density field, is optimized along with the sequence optimization. To account for this, the density distribution is factored in as a scaling factor with a penalization κ, in line with the power law relation between the stiffness and density in SIMP (Solid Isotropic Material with Penalization) [59]. This power law reduces the equivalent forces from elements with intermediate densities that appear in the optimization process before convergence. In this research, we choose $\kappa = 3$.

The incremental displacement of the entire domain induced by the inherent strain of the j-th layer is calculated by solving the linear elastic equation,

$$\mathbf{K}^{\{j\}} \Delta \mathbf{U}^{\{j\}} = \mathbf{F}^{\{j\}}. \tag{11}$$

Consequently, the residual stress corresponding to this displacement is calculated by

$$\Delta \sigma_e{}^{\{j\}} = \rho_e^{\{j\}^\kappa} \mathbf{D} \mathbf{B} \Delta \mathbf{U}_e{}^{\{j\}} - \eta_e^{\{j\}^\kappa} \mathbf{D} \boldsymbol{\varepsilon}^*. \tag{12}$$

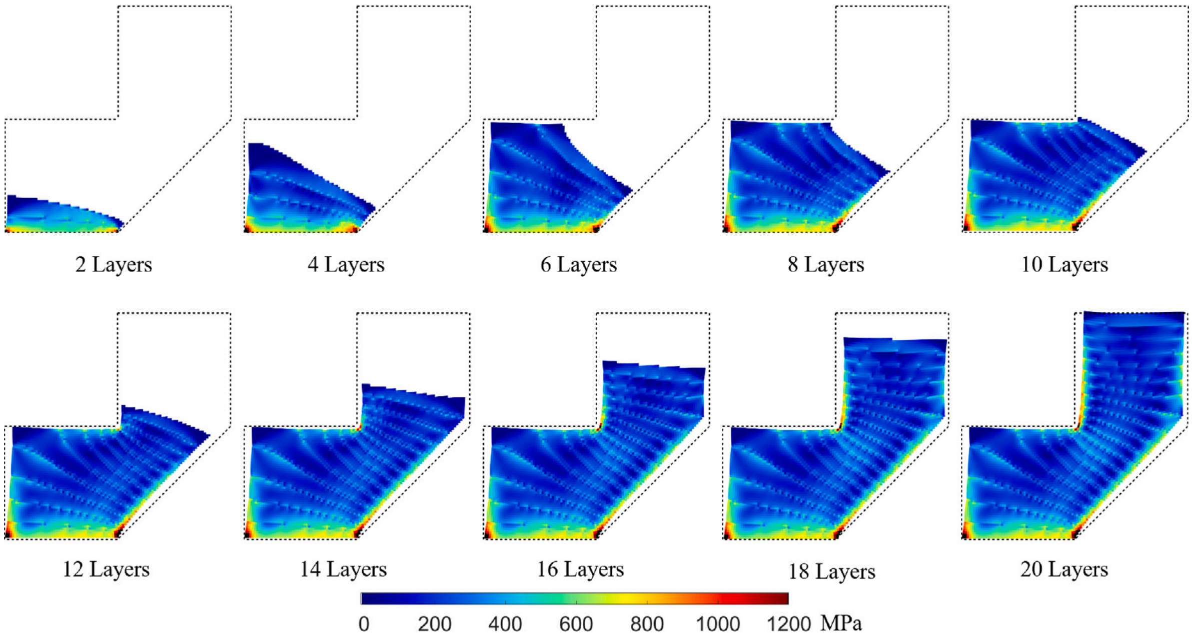

Fig. 3. Simulation of the layer-based manufacturing process, with the accumulation of residual stresses and distortions.

The residual stress consists of two parts. The first corresponds to the stress associated with the deformation induced by the new layer. It affects the intermediate structure $\boldsymbol{\rho}^{\{j\}}$. The second accounts for the release of the inherent stain. It mainly concerns the new layer $\boldsymbol{\eta}^{\{j\}}$.

It should be noted that the layers that have not been produced yet are also included in the analysis for calculating the distortion. Elements in the inactive layers are assigned a small density or Young's modulus to avoid the stiffness matrix from becoming singular. During manufacturing, each new layer is added in a stress-free state. To account for this stress-free initial state of a new layer, the first part in the residual stress (Eq. (12)) is scaled by the density, with a power law relation in consistency with that for the inherent strain.

The above formulations are applied to simulate the component and fabrication sequence illustrated in Fig. 1. Fig. 3 shows the accumulated deformations and residual stresses in a series of intermediate structures. To enhance visibility, a scaling factor is applied to exaggerate the displacements. Individual elements in the intermediate structures are colored by their von Mises residual stress. Significant residual stresses are observed at the bottom of the component, particularly on both sides, where it is attached to the baseplate. Additionally, a smaller stress concentration is noticeable around the right-angled corner in the middle of the component.

2.3. Residual stress constraint

We formulate residual stresses in a constraint in space–time topology optimization. Specifically, we consider the residual stress distribution after the entire component has been fabricated in this research. As our simulation results will show later, the residual stress during the manufacturing process will not significantly exceeds the final residual stress value. For future work, it also makes sense to further include layer-wise residual stresses constraints.

We follow established methods for handling the 'singularity' and large number of stress constraints in topology optimization. 'Singularity' refers to the situation where the global optimum is located in a lower dimensional subspace within the solution space, and cannot be reached using gradient-based optimization [55]. To cope with this problem, the idea is to relax the stress definition and thus the solution space. In our work, we adopt the qp-relaxation [56,57]:

$$\hat{\boldsymbol{\sigma}} = \boldsymbol{\rho}^{q}\boldsymbol{\sigma}, \tag{13}$$

where $\hat{\boldsymbol{\sigma}}$ is the relaxed stress. $\boldsymbol{\sigma}$ is the residual stress as calculated from Eq. (7). q is a relaxation parameter, and is set as $q = 0.5$.

We use the von Mises stress as the yielding criterion. For general plane stress condition, the von Mises stress ($\hat{\sigma}_{\mathrm{vM},e}$) is evaluated at each element

$$\hat{\sigma}_{\mathrm{vM},e} = \sqrt{\hat{\sigma}_{11,e}^2 + \hat{\sigma}_{22,e}^2 + 3\hat{\sigma}_{12,e}^2 - \hat{\sigma}_{11,e}\hat{\sigma}_{22,e}}, \tag{14}$$

where $\hat{\sigma}_{11,e}, \hat{\sigma}_{22,e}, \hat{\sigma}_{12,e}$ are components of the relaxed stress tensor. This equation is rewritten in matrix format to simplify sensitivity analysis:

$$\hat{\sigma}_{\mathrm{vM},e} = \left(\hat{\boldsymbol{\sigma}}_e^{\mathrm{T}}\mathbf{V}\hat{\boldsymbol{\sigma}}_e\right)^{1/2}, \tag{15}$$

where $\hat{\boldsymbol{\sigma}}_e$ is the vectorized residual stress tensor of element e, and matrix $\mathbf{V}$ is defined as

$$\mathbf{V} = \begin{bmatrix} 1 & -1/2 & 0 \\ -1/2 & 1 & 0 \\ 0 & 0 & 3 \end{bmatrix}, \tag{16}$$

Stress is a local measure and thus a constraint on stress shall be applied to each element. To reduce the large number of stress constraints, we use the p-norm to aggregate the residual stresses into one single global value $\sigma_{\mathrm{vM,P}}$:

$$\sigma_{\mathrm{vM,P}} = \left(\sum_e \hat{\sigma}_{\mathrm{vM},e}^p \right)^{\frac{1}{p}} \leq \sigma_{\mathrm{lim}}, \tag{17}$$

where p is the aggregation parameter. σ_{lim} is the stress limit, *e.g.*, the yield stress of the material. A large p value leads to a more accurate approximation of the maximum stress. However, it also implies a high nonlinearity. In this research, we choose $p = 10$ as a trade-off between ensuring adequate smoothness for good performance of the optimization algorithm and an adequate approximation.

To improve the approximation accuracy between the maximum stress and the p-norm, we adopt the normalization procedure as suggested by Le et al. [57]. A normalization parameter A^I is defined as follows,

$$A^I = \alpha \frac{\max \hat{\sigma}_{\mathrm{vM},e}}{\sigma_{\mathrm{vM,P}}} + (1-\alpha) A^{I-1}, \tag{18}$$

where α is a control parameter, chosen as 0.5 in this research. The parameter A^I, with the superscript indicating the Ith iteration, is updated at every iteration, partially using the information from the last iteration $(I-1)$. The constraint on the normalized residual stress is written as

$$g_s = A^I \sigma_{\mathrm{vM,P}} - \sigma_{\mathrm{lim}} \leq 0. \tag{19}$$

We note that A^I is not differentiable and is considered as a constant in each iteration. As the optimization progresses, the design changes between successive iterations become smaller. Consequently, the normalization parameter A^I stabilizes.

2.4. Residual stress-constrained space–time topology optimization

The constraint on residual stresses is incorporated into two optimization settings. In the first setting, only the fabrication sequence is optimized, while the structural layout of the component remains fixed. This is typical in the manufacturing industry where component designs are provided externally. In the second setting, both the structural layout and the fabrication sequence are optimized simultaneously. This approach reflects a more integrated design and fabrication process, offering greater flexibility.

2.4.1. Sequence optimization

The fabrication sequence optimization is formulated as follows,

$$\underset{\boldsymbol{\mu}}{\text{Minimize:}} \quad f_0 = \omega_1 c_{\mathrm{thermal}} + \omega_2 f_{\mathrm{geo}} \tag{20}$$

$$\text{Subject to:} \quad \mathbf{K}^{\{j\}} \Delta \mathbf{U}^{\{j\}} = \mathbf{F}^{\{j\}}, \quad j = 1, 2, \ldots, N, \tag{21}$$

$$\mathbf{K}_{\mathrm{T}} \mathbf{T} = \mathbf{b}, \tag{22}$$

$$g_j = \sum \rho_e^{\{j\}} v_e - \frac{j}{N} V_0 \leq 0, \quad j = 1, 2, \ldots, N, \tag{23}$$

$$g_s = A^I \sigma_{\mathrm{vM,P}} - \sigma_{\mathrm{lim}} \leq 0, \tag{24}$$

$$0 \leq \mu_e \leq 1. \tag{25}$$

The objective function comprises two terms, scaled by weight coefficients ω_1 and ω_2. The first term evaluates the deformation of the component caused by the successive release of layer-wise inherent strains. For demonstration purposes, we take inspiration from the static compliance used in conventional compliance minimization problems, and define this term as:

$$c_{\mathrm{thermal}} = \mathbf{U}_{\mathrm{thermal}}{}^{\mathrm{T}} \mathbf{K} \mathbf{U}_{\mathrm{thermal}}, \tag{26}$$

where $\mathbf{K}$ is the stiffness matrix of the complete component. $\mathbf{U}_{\mathrm{thermal}}$ is the accumulated displacement vector as defined in Eq. (6). This measure accounts for the deformation of all elements, and thus can be viewed as a global metric. Alternative distortion measures, such as the flatness of edges or surfaces that are important for assembly, can also be employed [36,41].

The second term in the objective function concerns variations in the layer geometry. The layers in the optimized fabrication sequence are typically curved, with a large variation of height (or thickness) within each layer. The large variation is less favorable from a manufacturing perspective. The term f_{geo} measures variations in each layer, by

$$f_{\mathrm{geo}} = \sum_{j=1}^{N} \sum_e \eta_e^{\{j\}^{\kappa}} \left(|\nabla t_e| - \overline{|\nabla t|}^{\{j\}} \right)^2, \tag{27}$$

where $|\nabla t_e|$ is the magnitude of the gradient of the time field at an element, and $\overline{|\nabla t|}^{\{j\}}$ is the averaged magnitude of gradients within the j-th layer, i.e.,

$$\overline{|\nabla t|}^{\{j\}} = \frac{\sum_e \eta_e^{\{j\}^{\kappa}} |\nabla t_e|}{\sum_e \eta_e^{\{j\}^{\kappa}}}. \tag{28}$$

It should be noted that f_{geo} does not guarantee a uniform layer thickness. In fact, variations in layer thickness offer the flexibility needed to form non-planar curved layers.

The optimization problem is subject to two sets of PDEs, both of which are discretized using finite element methods. Eq. (21) analyzes the incremental displacement on the intermediate structure under the equivalent load of inherent strains in each newly deposited layer. Eq. (22) is the discretized version of the virtual heat equation (Eq. (4)). In addition to the PDE constraints, g_j is the volume constraint for each layer, assuming a constant manufacturing speed — the same amount of material volume is processed at each time interval. V_0 is the total material volume. g_s is the global residual stress constraint as discussed in Section 2.3.

2.4.2. *Concurrent optimization of structural layout and fabrication sequence*

In the concurrent optimization setting, the structural layout is optimized as well. Here we consider design optimization of lightweight load-bearing structures. The structural performance and total material consumption are added to the formulation as constraints.

$$\text{Subject to:} \quad \mathbf{K}\mathbf{U} = \mathbf{F}, \tag{29}$$

$$g_c = \mathbf{U}^{\mathrm{T}}\mathbf{K}\mathbf{U} - c_{\text{lim}} \le 0, \tag{30}$$

$$g_0 = \sum \rho_e v_e - V_0 \le 0, \tag{31}$$

$$0 \le \phi_e \le 1. \tag{32}$$

Eq. (29) is the static equilibrium equation for the complete structure under external loads in its service condition. g_c sets an upper bound for the mechanical compliance, c_{lim}. Alternatively, this constraint can also be added into the objective function, with an additional weight coefficient. Lastly, g_0 is the global volume constraint, which limits the total amount of material used for the entire structure.

It should be noted that the pseudo-density field, $\boldsymbol{\rho}$, is not directly treated as design variables. Instead, we adopt the three-field approach commonly used in density-based topology optimization [60]. The design variables are represented by the design field $\boldsymbol{\phi}$, which is then smoothed through a convolution filter to obtain a filtered field, $\tilde{\boldsymbol{\phi}}$. This filtering prevents the occurrence of checkerboard patterns in the optimized structure. The filtered field $\tilde{\boldsymbol{\phi}}$ is subsequently transformed using a smoothed Heaviside function to promote a black-and-white design. This yields the pseudo-density field $\boldsymbol{\rho} = \bar{\tilde{\boldsymbol{\phi}}}$, which is used in the structural analysis that follows. For details about the transformations of optimization variables, readers are referred to Wu et al. [29],Wang et al. [41].

Both optimization problems are solved using gradient-based methods, specifically the method of moving asymptotes (MMA) [61]. A detailed sensitivity analysis is provided in Appendix A and Appendix B.

3. Numerical examples

In this section, we validate the proposed method using multiple numerical examples. We start with fabrication sequence optimization on an L-shaped component (Section 3.1) and a bracket (Section 3.2). Following that, we extend to simultaneous optimization of the structural layout and fabrication sequence, allowing for more flexibility (Section 3.3). The material used in these examples is titanium, with Young's modulus $E = 110\,\text{GPa}$ and Poisson's ratio $\nu = 0.3$. The residual stress limit is set as $\sigma_{\text{lim}} = 1200\,\text{MPa}$, while the inherent strain value is $\boldsymbol{\varepsilon}_0^* = \left[\epsilon_{xx}, \epsilon_{yy}, \epsilon_{xy}\right]^{\mathrm{T}} = [-0.00375, -0.00375, 0]^{\mathrm{T}}$, unless otherwise specified. The method is implemented in MATLAB, and the code has not been specifically optimized for computational efficiency. All simulations were executed on a single CPU core of a workstation equipped with an Intel Xeon E-2630v4 processor and 256 GB of RAM.

3.1. *Fabrication sequence optimization for a V-shaped component*

The first example for fabrication sequence optimization is a V-shaped component, shown in Fig. 4(a). The resolution of the background mesh is 100 × 100 elements. The baseplate for fabrication is located at the bottom of the component. In the manufacturing process simulation, the component is fixed at the bottom. The prescribed number of layers is 40. On average, each iteration in the optimization process takes 275.2 s.

Fig. 4 (top) presents simulation results for the component manufactured using planar layers. Fig. 4(b) displays the von Mises stress distribution of the total residual stresses in the final structure. It reveals a maximum residual stress of $\sigma_{\max} = 2551.1\,\text{MPa}$, which is 112.6% above the limit. The corresponding structural distortion is shown in Fig. 4(c), with a total thermal-induced compliance of 1.565×10^5 mJ. By comparison, the optimized fabrication sequence (Fig. 4, bottom) employs curved layers to mitigate these effects. The maximum residual stress is reduced to $\sigma_{\max} = 1200.4\,\text{MPa}$, numerically satisfying the stress constraint, while distortion decreases significantly to 8.327×10^4 mJ, a 46.8% reduction in compliance compared to the planar case.

From the residual stress distributions, high residual stresses can be observed at the two ends of the bottom and around the right-angled corner in the middle (marked as P_1, P_2, and P_3 in Fig. 4(a)). The histories of residual stresses at these three locations

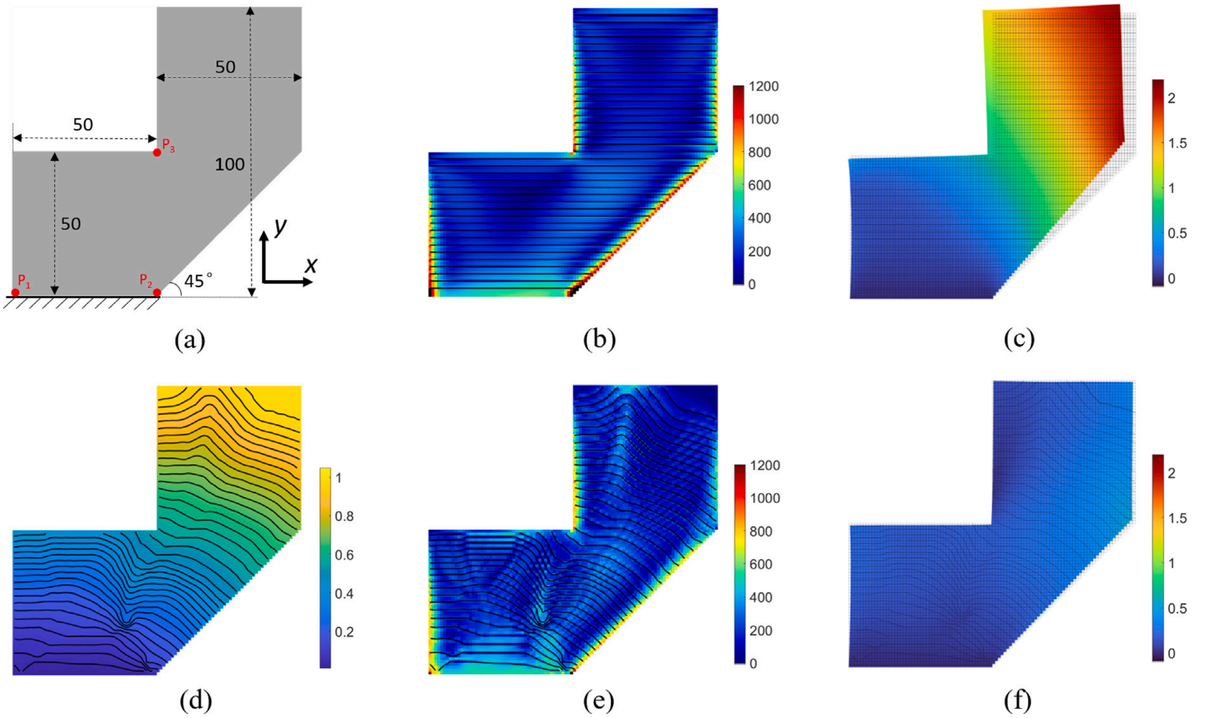

Fig. 4. Comparisons between planar and non-planar fabrication of a V-shaped component. (a) The dimensions of the V-shaped component. (b) The resulting residual stresses from planar fabrication. Elements with stresses exceeding the limit (σ_{lim} = 1200 MPa) are colored in black. (c) The corresponding structural distortion. (d) The optimized time field. Its isolines segment the component into curved layers. (e, f): Using curved fabrication, the resulting residual stresses (e) and distortion (f).

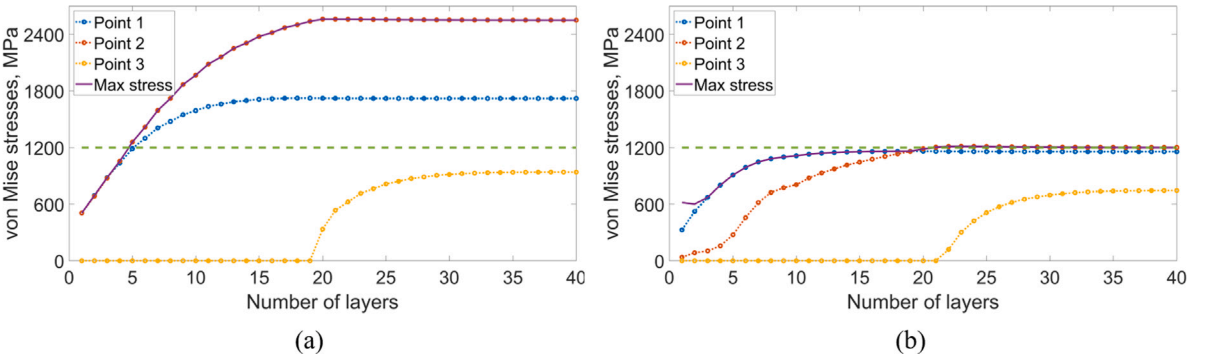

Fig. 5. The accumulation of residual stresses at three sampling points during the manufacturing process, according to the planar layers (a), and the optimized curved layers (b) shown in Fig. 4.

are plotted in Fig. 5, with the horizontal axis indicating the increasing number of layers during the manufacturing process. The subfigure on the left represents fabrication with planar layers, while the one on the right shows fabrication with optimized curved layers. When the component is manufactured using planar layers (Fig. 5(a)), the residual stresses at Point 1 and Point 2 increase gradually, both exceeding the stress limit of 1200 MPa after 5 layers. The stress at Point 3 appears after 19 layers and stops increasing at around 940 MPa until the end of fabrication. In contrast, when manufactured using optimized fabrication sequences (Fig. 5(b)), the increases of residual stresses at Point 1 and Point 2 are suppressed. The residual stress at Point 1 remains below the stress limit, with a margin of 40 MPa. While the residual stress at Point 2 increases to slightly over the stress limit after 20 layers, it returns to the limit onwards. The stress at Point 3 appears after 21 layers and reaches around 750 MPa at the end of fabrication. This demonstrates the effectiveness of the residual stress constraint. We note that this constraint is applied to the residual stresses at the completion of fabrication (i.e., after 40 layers). During the manufacturing process, the maximum residual stress does not significantly exceed the limit, so the residual stress history is not included in the optimization. However, in principle, it could be included, though at the cost of increasing the number of residual stress constraints by considering the stresses of all intermediate structures.

Table 1
Results of the V-shaped component with different fabrication sequences.

		Optimization result with differential layers		Post-analysis with binary layers	
		Maximum stress	Thermal compliance	Maximum stress	Thermal compliance
$N = 40$	Planar layers	2551.1 MPa	1.565×10^5 mJ	2709.3 MPa	1.435×10^5 mJ
	Optimized curved layers	1200.4 MPa	8.327×10^4 mJ	1276.0 MPa	8.396×10^4 mJ

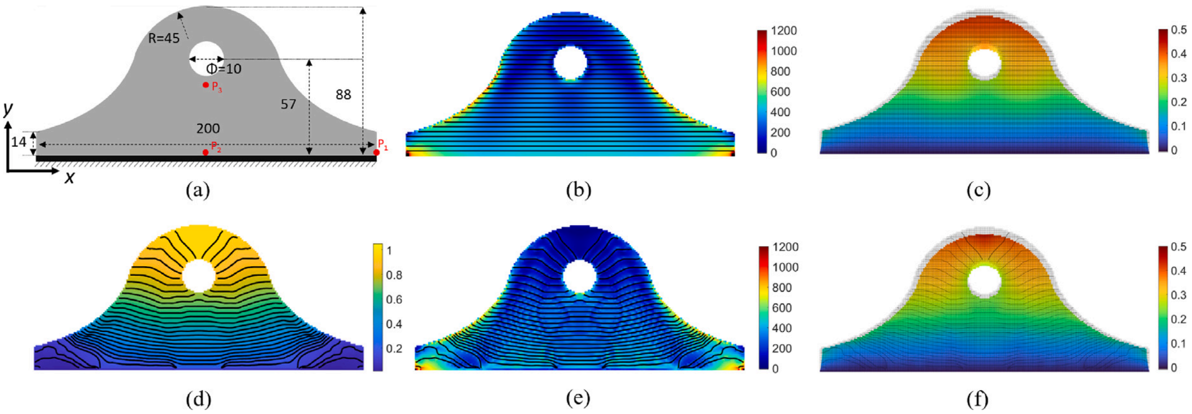

Fig. 6. Comparisons between planar and non-planar fabrication on a symmetric bracket, with 30 layers. (a) The geometry of the bracket. (b, c): Using planar fabrication, the resulting residual stresses (b) and distortion (c). (d) The optimized time field. Its isolines segment the component into curved layers. (e, f): Using curved fabrication, the resulting residual stresses (e) and distortion (f).

We further analyze the effects of approximating discrete manufacturing processes with a differential formulation that facilitates gradient-based optimization. To this end, we perform a post-optimization analysis of the optimized sequence, adopting the binary layer description defined in Eq. (1). The maximum residual stresses and thermal-induced compliances in the optimization and the post-analysis are summarized in Table 1. Specifically, for the optimized layers, post-analysis reveals an increase in the maximum residual stress from 1200.4 MPa to 1276.0 MPa, i.e., an increase of 6.30%. The thermal-induced compliance is increased from 8.327×10^4 mJ to 8.396×10^4 mJ, i.e., an increase of 0.83%. A similar trend is observed for the planar layers, which in the continuous formulation were defined by a height field, i.e., $t_e = \frac{y_e}{Y}$, where y_e is the y-coordinate of the element's centroid, and Y is the height of the component. The difference between the differential and binary layer descriptions comes from grey elements in the intermediate structures $\rho^{\{j\}}$. The discrepancies are small, thanks to the continuation scheme for the projection parameter β_t in the smoothed Heaviside projection. To account for the unavoidable discrepancies due to the continuous approximation of a discrete manufacturing process, one could set a tighter residual stress limit in the constraint, i.e., reducing σ_{lim} to e.g., 1100 MPa.

3.2. Fabrication sequence optimization for a bracket

The second example is a bracket, shown in Fig. 6(a). The resolution of the background mesh is 200×88. During manufacturing, the component is fully fixed at the bottom, where the fabrication starts. Fig. 6(b) and (c) show the resulting residual stress and distortion, respectively, if the component is fabricated with 30 planar layers. The maximum residual stress in the final structure is $\sigma_{\max} = 1950.5$ MPa, exceeding the stress limit by 62.54%. The thermal-induced compliance is 6.786×10^4 mJ. The bottom row of Fig. 6 shows, from left to right, the optimized curved layers, corresponding residual stress distribution, and distortion. The curved layers are optimized to minimize the thermal-induced compliance under a constraint on residual stresses. With the curved layers, the maximum residual stress is reduced to $\sigma_{\max} = 1199.6$ MPa.

To help understand how the curved layers avoid high residual stresses, Fig. 7 presents the sequence of the first 8 layers. From the first layer, it can be seen that the fabrication starts from the two sides at the bottom. Compared to a planar first layer, this reduces the length of the material deposition area, and thus leads to less accumulation of residual stress on the left and right corners.

It is noticed that while the residual stress is effectively constrained by the curved layers, the corresponding thermal-induced distortion increases by 7.38%, to 7.287×10^4 mJ. It shall be noted the bracket is considered suitable for planar fabrication thanks to its symmetric geometry and the presence of only a small overhang at the top of the inner ring. In planar fabrication, the thermal-induced distortion of the bracket is rather smaller than that of the L-shaped component. The symmetry of the bracket allows distortions from both sides to cancel each other out. However, this suppression of distortion through symmetry results in high residual stresses, which must be mitigated. Curved fabrication offers an effective solution for reducing these stresses.

Fig. 8(a) plots the history of residual stresses at three critical points when the component is fabricated with the curved layers. The locations of these three points are marked in Fig. 6(a). The residual stresses at all three points monotonically increase during manufacturing, with the point on the end at the bottom showing the highest residual stress. In addition, the convergence history

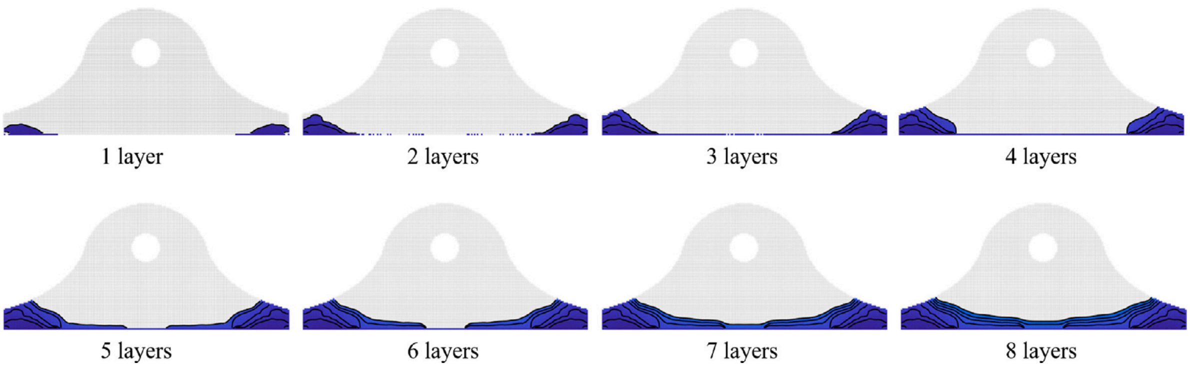

Fig. 7. Illustration of the first 8 layers in manufacturing the bracket according to the optimized fabrication sequence.

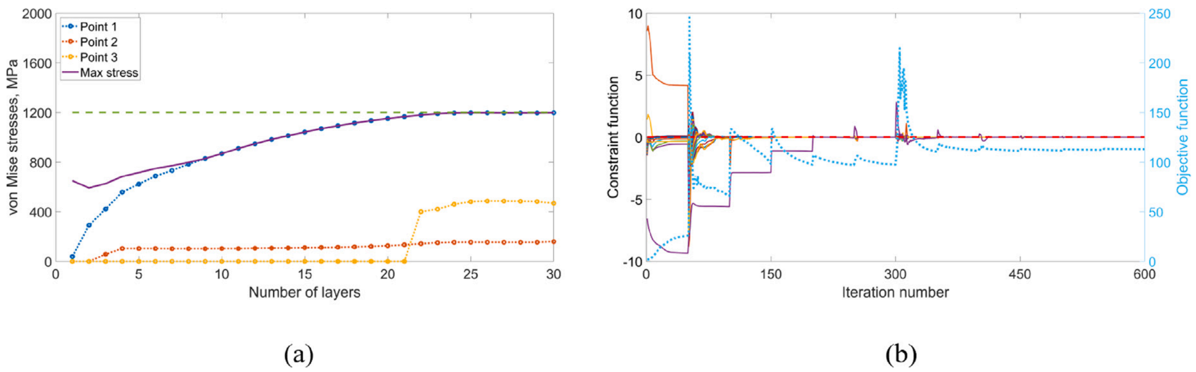

Fig. 8. Data analysis for the bracket component. (a) The accumulation of residual stresses at three sampling points during manufacturing. (b) Convergence of the objective function (dotted line in light blue) and the constraint functions. (For interpretation of the references to color in this figure legend, the reader is referred to the web version of this article.)

Table 2
Results of the bracket with planar and curved fabrication.

		Optimization result with differential layers		Post-analysis with binary layers	
		Maximum stress	Thermal compliance	Maximum stress	Thermal compliance
$N = 30$	Planar layers	1950.5 MPa	6.786×10^4 mJ	1997.1 MPa	6.147×10^4 mJ
	Optimized curved layers	1199.6 MPa	7.287×10^4 mJ	1250.8 MPa	7.119×10^4 mJ
$N = 10$	Planar layers	1649.3 MPa	5.313×10^4 mJ	1655.6 MPa	5.097×10^4 mJ
	Optimized curved layers	1201.0 MPa	5.592×10^4 mJ	1251.5 MPa	5.124×10^4 mJ

of the objective function and the constraint functions are shown in Fig. 8(b). All the constraint functions converge to zero, and the objective function converges stably. The initial time field is solved from a uniform heat conductivity field, leading to a low objective value but significant violations of the constraints. As the constraints are gradually satisfied, the objective value increases. Notably, abrupt changes in the convergence curve occur every 50 iterations, which are due to the continuation scheme applied to the projection parameter β_t.

To investigate the influence of the number of layers, we also optimized the fabrication sequence with a reduced number of layers, i.e., from 30 to 10. Consequently, the average computation time per iteration is reduced from 228 s to 84 s, achieving a 2.7-fold speedup, which aligns with the threefold reduction in the number of mechanical analyses. The simulation results of the planar layers and optimized curved layers are shown in the top and bottom rows of Fig. 9, respectively. The maximum residual stress and thermal-induced compliance are summarized in Table 2. With 10 planar layers, both the maximum residual stress and the thermal-induced compliance were reduced, in comparison to 30 planar layers. The optimized curved fabrication, with 10 layers, is again effective in restricting the maximum residual stress. However, when the number of layer divisions decreases, the design freedom for fabrication sequence is restricted. The entire bottom edge has to be built within the first single layer, as there are only 10 layers in total. The appropriate number of layers shall be chosen based on the experimental setup, particularly considering the layer thickness.

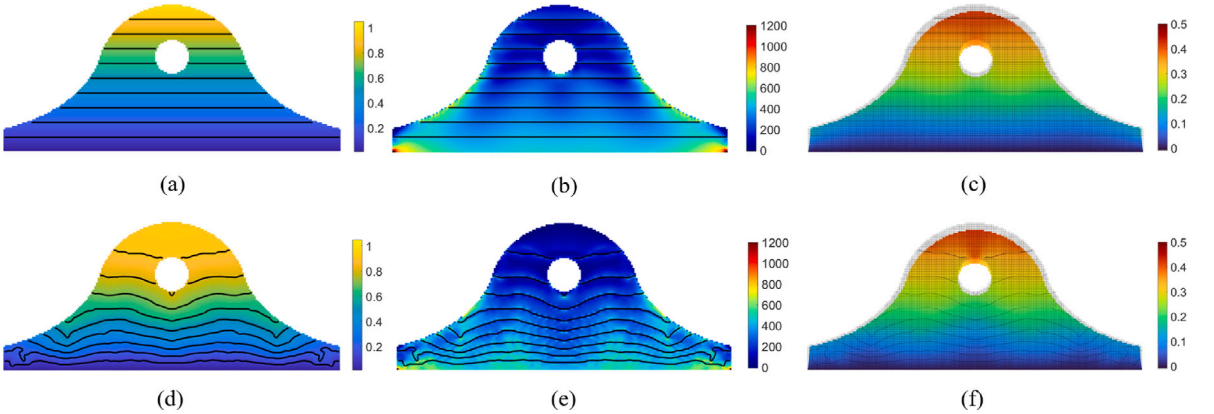

Fig. 9. Comparisons between planar and non-planar fabrication on a symmetric bracket, with 10 layers. (a) The planar layers. (b, c): Using planar fabrication, the resulting residual stresses (b) and distortion (c). (d) The optimized time field. Its isolines segment the component into curved layers. (e, f): Using curved fabrication, the resulting residual stresses (e) and distortion (f).

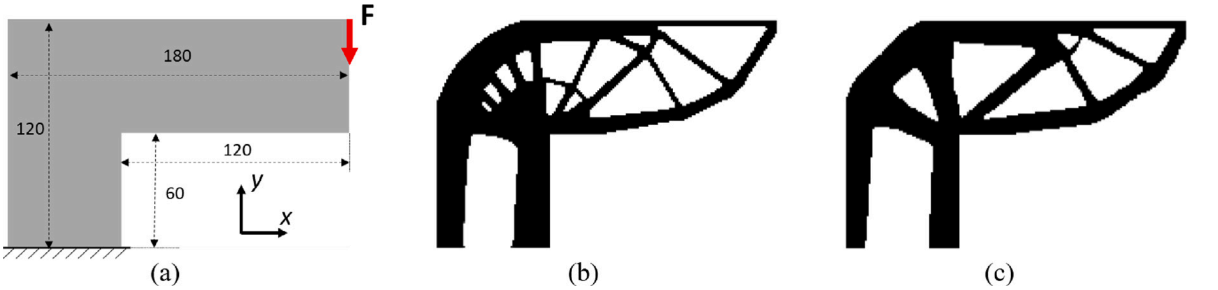

Fig. 10. Structural optimization of the L-shaped component. (a) The design domain and boundary condition of the L-shaped component. (b) The optimized structure when the structural layout and fabrication sequence are simultaneously optimized. (c) The optimized structure from standard topology optimization.

3.3. Concurrent structural and sequence optimization for the L-shaped component

In our last example, we validate the concurrent optimization of the structural layout and the fabrication sequence. The L-shaped component shown in Fig. 10(a) serves as the design domain. The domain is discretized using a grid of 180 × 120 elements. In structural optimization, the material volume ratio is restricted to 0.5, and an external force is applied on the top right corner. As the total amount of material is reduced by half, less energy is introduced into the structure during fabrication, and thus small residual stresses and distortions. To demonstrate the effectiveness of the optimization, we doubled the inherent strain value in order to amplify the resulting residual stresses: $\epsilon_0^* = \left[\epsilon_{xx}, \epsilon_{yy}, \epsilon_{xy}\right]^{\mathrm{T}} = [-0.0075, -0.0075, 0]^{\mathrm{T}}$. In the simulation of the fabrication process, the component is fixed at the bottom. The total number of layers is prescribed to 20. The average computation time per iteration is 240 s.

Fig. 10(b) shows the structural layout from space–time topology optimization. As a reference, the layout from the standard topology optimization (i.e., no consideration of the manufacturing process) is shown in Fig. 10(c). Both optimizations lead to clear structural layouts. The external boundaries of the two designs are fairly similar, while the internal structures from the standard topology optimization are less complex. In standard topology optimization, the objective is to minimize compliance, which is reduced 2170.4 mJ in this case. Taking this value as a reference, the compliance limit is set to 2200.0 mJ in space–time topology optimization, in which compliance is treated as a constraint (Eq. (30)). This constraint function is numerically satisfied in the optimization process, leading to a compliance of 2202.8 mJ.

The corresponding fabrication sequence optimized from space–time topology optimization is shown in Fig. 11(g). For comparison, two planar fabrication sequences for the same structural layout are included: horizontal layers (a), and layers inclined at 45°(f). The residual stress distributions for all three sequences (horizontal, inclined, and optimized) are shown in the middle column of each row, while thermal-induced distortions are illustrated on the right. As summarized in Table 3, both horizontal and inclined layers result in the maximum stress above the limit, while by the optimized curved layers the maximum is reduced to 1211.1 MPa. Converting the grey values in the differentiable layer formulation to binary layers, the maximum residual stresses are 1352.3 MPa, 1410.9 MPa and 1189.0 MPa for the three fabrication sequences respectively. The optimized sequence reduces the maximum residual stress by more than 12%. More pronouncedly, the thermal-induced distortion is reduced from 5.207×10^5 mJ to 2.168×10^5 mJ, a reduction of 58.36%.

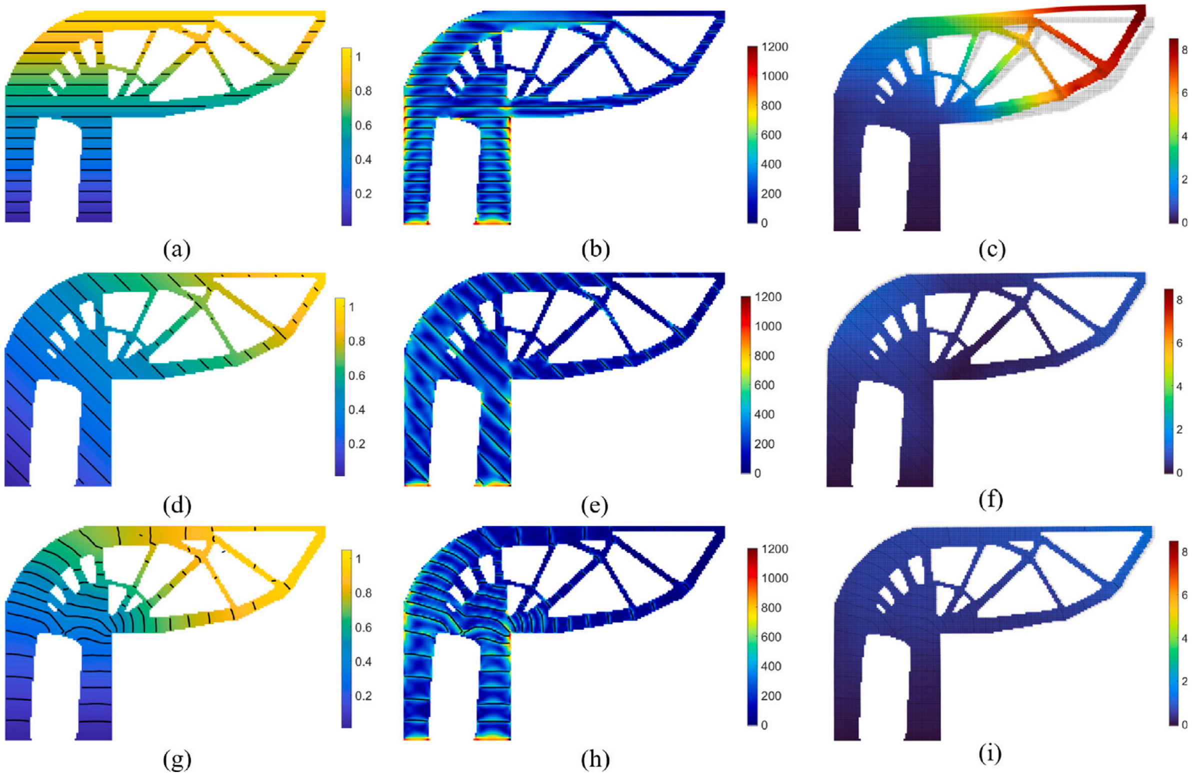

Fig. 11. The simultaneously optimized structure (Fig. 10(b)) and sequence are compared to the same structure but with planar layers. (a) The horizontal planar layers. (b, c): Using horizontal layers, the resulting residual stresses (b) and distortion (c). (d, e, f): The inclined layers and corresponding stresses and distortion. (g, h, i) Curved layers from the simultaneously optimized time field, and the corresponding stresses and distortion.

Table 3
Results of the L-shaped component with different structural layouts and fabrication sequences, $N = 20$.

	Compliance	Fabrication sequence	Maximum stress		Thermal compliance	
			Differential	Binary	Differential	Binary
Simultaneous optimization	2202.8 mJ	Horizontal layers	1324.7 MPa	1352.3 MPa	5.819×10^5 mJ	5.207×10^5 mJ
		Inclined layers	1308.4 MPa	1410.9 MPa	3.204×10^5 mJ	2.794×10^5 mJ
		Curved layers	1211.1 MPa	1189.0 MPa	2.284×10^5 mJ	2.168×10^5 mJ
Sequential optimization	2170.4 mJ	Horizontal layers	1369.2 MPa	1410.6 MPa	6.041×10^5 mJ	5.422×10^5 mJ
		Inclined layers	1263.1 MPa	1359.5 MPa	2.831×10^5 mJ	2.592×10^5 mJ
		Curved layers	1200.1 MPa	1200.8 MPa	2.139×10^5 mJ	1.957×10^5 mJ

A further comparison is made on the structural layout from the standard topology optimization, shown in Fig. 10(c). The first two rows show results for horizontal and inclined layers (45°). The bottom row shows the results of the fabrication sequence optimization of the topology-optimized structure—The sequence optimization is performed after the structural optimization, rather than concurrently. Compared to planar manufacturing strategies, the optimized fabrication sequence effectively reduces both the maximum residual stress and thermal-induced distortion, aligning with trends observed in earlier examples.

An interesting observation arises from comparing the sequential optimization (Fig. 12, bottom) with the concurrent optimization (Fig. 11, bottom). The numerical values for these two scenarios, summarized in Table 3, differ only marginally, which was somewhat unexpected but not entirely surprising. This can be attributed to the large number of variables involved in sequence optimization, which results in a vast solution space even when the structure is fixed. Additionally, the search within the even larger solution space in concurrent structural and sequence optimization is mathematically more complicated. Furthermore, structural and fabrication sequence optimizations have distinct objectives, which are integrated into the concurrent optimization in a mixed approach—structural compliance in a constraint, while distortion is part of the objective.

Lastly, the convergence history in the concurrent optimization for the L-shaped beam is plotted in Fig. 13. The layouts at the 100-th, 200-th, 300-th, 400-th iterations are included, to depict its evolution during optimization. The structural layout converges to a black-and-white design after about 300 iterations. The constraint functions all reduce to zero. The objective function reduces gradually, despite spikes due to a parameter continuation as previously explained. The layer-by-layer manufacturing process of the optimized L-shaped component is displayed in Fig. 14.

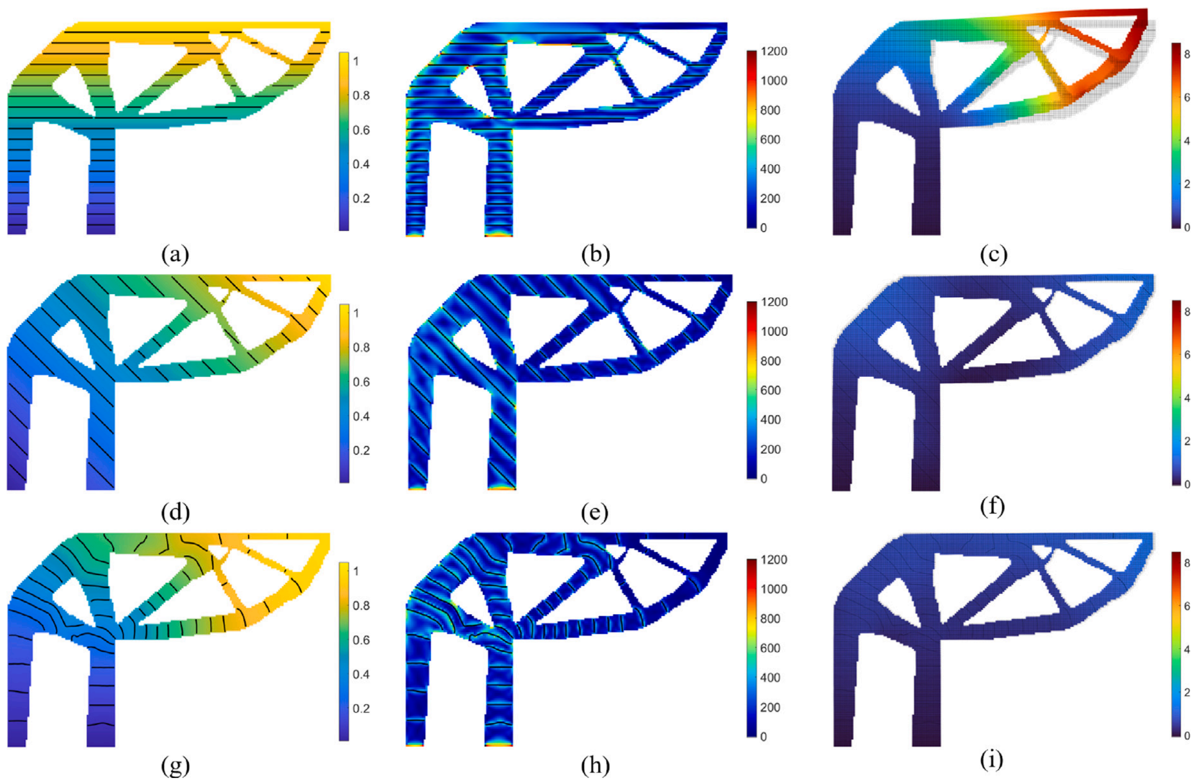

Fig. 12. Comparisons between horizontal (top), inclined (middle), and curved layers (bottom), tested on the structure from standard topology optimization (Fig. 10(c)). From left to right: layers, residual stresses, and distortions..

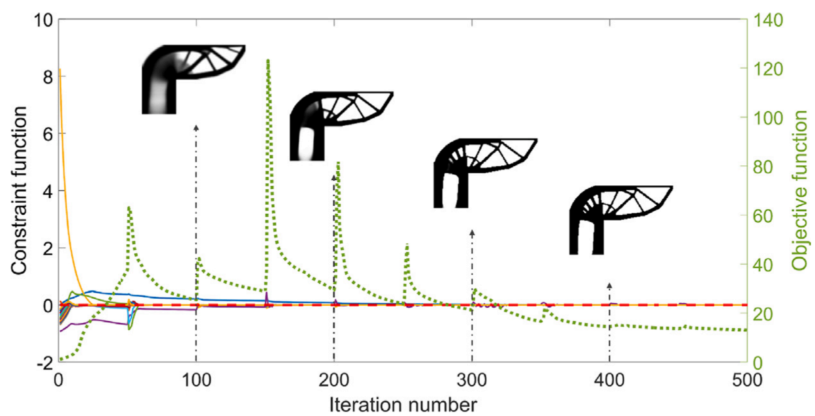

Fig. 13. Convergence of the objective and constraint functions in simultaneous optimization of the structural layout and fabrication sequence. The evolving structural layouts at the 100-th, 200-th, 300-th, 400-th iterations are included.

4. Conclusion

This paper introduces a novel method for reducing residual stresses in wire arc additive manufacturing. Our method optimizes the fabrication sequence, represented as isolines of a pseudo-time field. The optimization integrates residual stresses as a constraint while minimizing thermally induced distortions. The resulting sequences are predominantly curved, with smoothly varying orientations. Compared to traditional planar layers, the optimized curved layers significantly reduce distortion and effectively control excessive residual stresses. Additionally, the method allows for simultaneous optimization of both the fabrication sequence and the structural layout, offering valuable insights into how these factors influence residual stresses.

This work introduces fabrication sequence optimization as a new approach for enhancing the quality of WAAM and opens up several avenues for future exploration. Firstly, the inherent strain model could be replaced with high-fidelity process models to

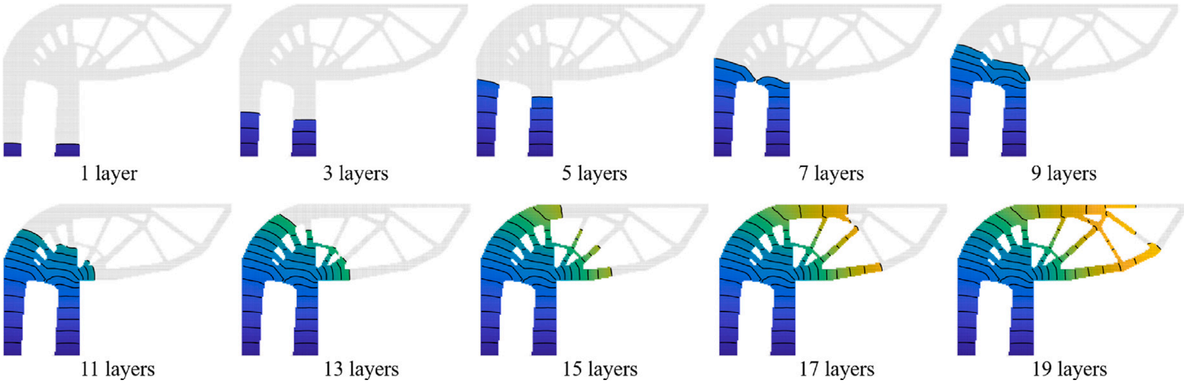

Fig. 14. Illustration of the fabrication process of the optimized structure with curved layers. For simplicity, only odd-numbered layers are included.

enhance the accuracy of residual stress and distortion predictions. Additionally, application-specific criteria (such as the Tsai–Wu failure criterion instead of von Mises stresses, or distortion metrics targeting critical geometric features like the flatness of assembly surfaces) could refine optimization outcomes. Furthermore, future work could explore tailoring the residual stress distribution, to improve the component strength under in-service mechanical loads. Last but not least, a key next step is the transition from numerical simulations to experimental validation, which is critical for industrial adoption. While the numerical results demonstrate considerable promise, practical realization through robotic systems for curved layer fabrication presents new challenges. For instance, while layers with varying thickness can be achieved by adjusting manufacturing process parameters, manufacturing practice favors curved layers with minimal thickness variation to ensure consistent print quality. Furthermore, the varying process parameters need to be incorporated into the process model. By addressing these challenges, this framework holds the potential to advance WAAM as a robust and reliable technology, enabling innovative applications across industries.

CRediT authorship contribution statement

Kai Wu: Writing – original draft, Visualization, Validation, Software, Methodology, Investigation, Formal analysis, Data curation, Conceptualization. **Fred van Keulen:** Writing – review & editing, Supervision, Resources, Project administration. **Jun Wu:** Writing – review & editing, Supervision, Resources, Funding acquisition, Conceptualization.

Declaration of competing interest

The authors declare that they have no known competing financial interests or personal relationships that could have appeared to influence the work reported in this paper.

Acknowledgments

The authors would like to thank Dr. Can Ayas, Dr. Dirk Munro, Dr. Weiming Wang, Dr. Vibhas Mishra, and Mr. Manabendra Nath Das for their valuable suggestions during our discussion. Kai Wu is supported by China Scholarship Council (No. 202006210069). This work is partly supported by the Dutch Research Council (NWO), Netherlands with project number 20382, "Space–time optimization for additive manufacturing".

Appendix A. Sensitivity analysis of the residual stress constraint

The residual stress constraint g_s is determined by optimization variables $\boldsymbol{\phi}$ and $\boldsymbol{\mu}$ via two intermediate fields, the density field $\boldsymbol{\rho} = \bar{\tilde{\boldsymbol{\phi}}}$, and the time field $\boldsymbol{t}$:

$$g_s(\boldsymbol{\phi}, \boldsymbol{\mu}) = g_s(\boldsymbol{\rho}, \boldsymbol{t}(\boldsymbol{\rho}, \boldsymbol{\mu})). \tag{33}$$

The time field depends on both the density field $\boldsymbol{\rho}$ and the thermal diffusivity field $\boldsymbol{\mu}$ by solving the heat equation.

Sensitivity w.r.t design variable $\boldsymbol{\phi}$. The design field $\boldsymbol{\phi}$ is filtered and then projected to obtain the density field $\boldsymbol{\rho}$. According to the chain rule, we have

$$\frac{\partial g_s}{\partial \phi_e} = \sum_{i \in \mathcal{N}_e} \frac{\mathrm{d} g_s}{\mathrm{d} \rho_i} \frac{\partial \bar{\tilde{\phi}}_i}{\partial \tilde{\phi}_i} \frac{\partial \tilde{\phi}_i}{\partial \phi_e}, \tag{34}$$

The sensitivity regarding the filtering and projection operations is routine. We focus on the derivative of the constraint function g_s with respect to the density $\boldsymbol{\rho}$.

The residual stress constraint g_s contains $\boldsymbol{\rho}$ explicitly, as well as implicitly through the time field. The density field is involved in defining the time field using a heat equation. An adjoint analysis is thus performed:

$$\begin{aligned}\frac{\mathrm{d}g_s}{\mathrm{d}\rho_i} &= \frac{\partial g_s}{\partial \rho_i} + \frac{\partial g_s}{\partial \mathbf{t}}\frac{\partial \mathbf{t}}{\partial \rho_i} + \boldsymbol{\lambda}_{\mathbf{T}}^{\top}\left(\frac{\partial \mathbf{b}}{\partial \rho_i} - \frac{\partial \mathbf{K}_{\mathrm{T}}}{\partial \rho_i}\mathbf{T} - \mathbf{K}_{\mathrm{T}}\frac{\partial \mathbf{T}}{\partial \rho_i}\right),\\ &= \frac{\partial g_s}{\partial \rho_i} - \frac{\partial g_s}{\partial \mathbf{t}}\frac{\partial \mathbf{T}}{\partial \rho_i} + \boldsymbol{\lambda}_{\mathbf{T}}^{\top}\left(-\frac{\partial \mathbf{K}_{\mathrm{T}}}{\partial \rho_i}\mathbf{T} - \mathbf{K}_{\mathrm{T}}\frac{\partial \mathbf{T}}{\partial \rho_i}\right),\\ &= \frac{\partial g_s}{\partial \rho_i} - \left(\frac{\partial g_s}{\partial \mathbf{t}} + \boldsymbol{\lambda}_{\mathbf{T}}^{\top}\mathbf{K}_{\mathrm{T}}\right)\frac{\partial \mathbf{T}}{\partial \rho_i} - \boldsymbol{\lambda}_{\mathbf{T}}^{\top}\frac{\partial \mathbf{K}_{\mathrm{T}}}{\partial \rho_i}\mathbf{T}.\end{aligned} \tag{35}$$

The Lagrange multiplier $\boldsymbol{\lambda}_{\mathbf{T}}$ is solved from

$$\frac{\partial g_s}{\partial \mathbf{t}} + \boldsymbol{\lambda}_{\mathbf{T}}^{\top}\mathbf{K}_{\mathrm{T}} = \mathbf{0}. \tag{36}$$

The calculation of $\frac{\partial g_s}{\partial \mathbf{t}}$ will be presented shortly. With that, the sensitivity of the constraint function is simplified into

$$\frac{\mathrm{d}g_s}{\mathrm{d}\rho_i} = \frac{\partial g_s}{\partial \rho_i} - \boldsymbol{\lambda}_{\mathbf{T}}^{\top}\frac{\partial \mathbf{K}_{\mathrm{T}}}{\partial \rho_i}\mathbf{T}. \tag{37}$$

The residual stress contains the accumulation of $\Delta\mathbf{U}^{\{j\}}$, which is solved from the linear equation of each intermediate structure as in Eq. (21). A set of adjoint analyses is needed accordingly for the calculation of $\frac{\partial g_s}{\partial \rho_i}$:

$$g_s = g_s + \sum_j \boldsymbol{\lambda}^{\{j\}}\left(\mathbf{K}^{\{j\}}\Delta\mathbf{U}^{\{j\}} - \mathbf{F}^{\{j\}}\right). \tag{38}$$

Its derivative with respect to the density of the ith element ρ_i is:

$$\frac{\partial g_s}{\partial \rho_i} = \frac{\partial g_s}{\partial \rho_i} + \sum_j \boldsymbol{\lambda}^{\{j\}}\left(\frac{\partial \mathbf{K}^{\{j\}}}{\partial \rho_i}\Delta\mathbf{U}^{\{j\}} + \mathbf{K}^{\{j\}}\frac{\partial \Delta\mathbf{U}^{\{j\}}}{\partial \rho_i} - \frac{\partial \mathbf{F}^{\{j\}}}{\partial \rho_i}\right). \tag{39}$$

Substituting g_s using Eq. (24) gives

$$\frac{\partial g_s}{\partial \rho_i} = A^I\left(\sum_e \hat{\sigma}_{\mathrm{vM},e}^p\right)^{\frac{1-p}{p}}\left(\sum_e \hat{\sigma}_{\mathrm{vM},e}^{p-1}\frac{\partial \hat{\sigma}_{\mathrm{vM},e}}{\partial \rho_i}\right), \tag{40}$$

where $\frac{\partial \hat{\sigma}_{\mathrm{vM},e}}{\partial \rho_i}$ is derived according to Eq. (15)

$$\frac{\partial \hat{\sigma}_{\mathrm{vM},e}}{\partial \rho_i} = \frac{\hat{\boldsymbol{\sigma}}_e^{\mathrm{T}}\mathbf{V}\frac{\partial \hat{\boldsymbol{\sigma}}_e}{\partial \rho_i}}{\hat{\sigma}_{\mathrm{vM},e}}. \tag{41}$$

Here the relaxed stress $\hat{\boldsymbol{\sigma}}_e$ is calculated according to Eq. (13), and thus

$$\frac{\partial \hat{\boldsymbol{\sigma}}_e}{\partial \rho_i} = \frac{\partial \boldsymbol{\sigma}_e}{\partial \rho_i}{\rho_e}^q + \frac{\partial \rho_e^q}{\partial \rho_i}\boldsymbol{\sigma}_e, \tag{42}$$

The next key step is to calculate the derivative of the stress $\boldsymbol{\sigma}_e$ with respect to the density ρ_i, according to Eqs. (7) and (12),

$$\begin{aligned}\frac{\partial \boldsymbol{\sigma}_e}{\partial \rho_i} &= \sum_j \frac{\partial \Delta{\boldsymbol{\sigma}_e}^{\{j\}}}{\partial \rho_i}\\ &= \sum_j\left(\mathbf{DB}\frac{\partial \Delta\mathbf{U}_e^{\{j\}}}{\partial \rho_i}R_E(\rho_e^{\{j\}}) + \mathbf{DB}\Delta\mathbf{U}_e^{\{j\}}\frac{\partial R_E(\boldsymbol{\rho}^{\{j\}})}{\partial \rho_i} - \mathbf{D}\boldsymbol{\varepsilon}^*\frac{\partial R_B(\eta_e^{\{j\}})}{\partial \rho_i}\right).\end{aligned} \tag{43}$$

By summarizing the above equations, Eq. (39) can be rewritten:

$$\begin{aligned}\frac{\partial g_s}{\partial \rho_i} =& A^I\left(\sum_e \hat{\sigma}_{\mathrm{vM},e}^p\right)^{\frac{1-p}{p}}\sum_e\left[\hat{\sigma}_{\mathrm{vM,e}}^{p-2}\cdot\left({\hat{\boldsymbol{\sigma}}_e}^{\mathrm{T}}\mathbf{VD}\sum_j\left(\mathbf{B}\frac{\partial \Delta\mathbf{U}_e^{\{j\}}}{\partial \rho_i}R_E(\rho_e^{\{j\}}) + \mathbf{B}\Delta\mathbf{U}_e^{\{j\}}\frac{\partial R_E(\rho_e^{\{j\}})}{\partial \rho_i} - \boldsymbol{\varepsilon}^*\frac{\partial R_B(\eta_e^{\{j\}})}{\partial \rho_i}\right)\rho_e^q\right.\right.\\ &\left.\left.+{\hat{\boldsymbol{\sigma}}_e}^{\mathrm{T}}\mathbf{V}\boldsymbol{\sigma}_e\frac{\partial \rho_e^q}{\partial \rho_i}\right)\right] + \sum_j \boldsymbol{\lambda}^{\{j\}}\left(\frac{\partial \mathbf{K}^{\{j\}}}{\partial \rho_i}\Delta\mathbf{U}^{\{j\}} + \mathbf{K}^{\{j\}}\frac{\partial \Delta\mathbf{U}^{\{j\}}}{\partial \rho_i} - \frac{\partial \mathbf{F}^{\{j\}}}{\partial \rho_i}\right),\end{aligned} \tag{44}$$

$$\begin{aligned}=& A^I\left(\sum_e \hat{\sigma}_{\mathrm{vM},e}^p\right)^{\frac{1-p}{p}}\sum_j\sum_e\left[\hat{\sigma}_{\mathrm{vM,e}}^{p-2}\rho_e^q\cdot{\hat{\boldsymbol{\sigma}}_e}^{\mathrm{T}}\mathbf{VD}\left(\mathbf{B}\frac{\partial \Delta\mathbf{U}_e^{\{j\}}}{\partial \rho_i}R_E(\rho_e^{\{j\}}) + \mathbf{B}\Delta\mathbf{U}_e^{\{j\}}\frac{\partial R_E(\rho_e^{\{j\}})}{\partial \rho_i} - \boldsymbol{\varepsilon}^*\frac{\partial R_B(\eta_e^{\{j\}})}{\partial \rho_i}\right)\right]\\ &+ A^I\left(\sum_e \hat{\sigma}_{\mathrm{vM},e}^p\right)^{\frac{1-p}{p}}\sum_e\left(\hat{\sigma}_{\mathrm{vM},e}^{p-2}{\hat{\boldsymbol{\sigma}}_e}^{\mathrm{T}}\mathbf{V}\boldsymbol{\sigma}_e\frac{\partial \rho_e^q}{\partial \rho_i}\right) + \sum_j \boldsymbol{\lambda}^{\{j\}}\left(\frac{\partial \mathbf{K}^{\{j\}}}{\partial \rho_i}\Delta\mathbf{U}^{\{j\}} + \mathbf{K}^{\{j\}}\frac{\partial \Delta\mathbf{U}^{\{j\}}}{\partial \rho_i} - \frac{\partial \mathbf{F}^{\{j\}}}{\partial \rho_i}\right).\end{aligned} \tag{45}$$

There are N Lagrangian equations to be solved in total:

$$A^I\left(\sum_e \hat{\sigma}_{\mathrm{vM},e}^p\right)^{\frac{1-p}{p}}\left(\sum_e \hat{\sigma}_{\mathrm{vM,e}}^{p-2}\rho_e^q R_E(\rho_e^{\{j\}})\cdot{\hat{\boldsymbol{\sigma}}_e}^{\mathrm{T}}\mathbf{VDB}\right) + \boldsymbol{\lambda}^{\{j\}}\mathbf{K}^{\{j\}} = 0. \tag{46}$$

After calculating the Lagrangian multipliers $\boldsymbol{\lambda}^{\{j\}}$, Eq. (39) is further simplified,

$$\frac{\partial g_s}{\partial \rho_i} = A^I \left(\sum_e \hat{\sigma}^p_{\mathrm{vM},e} \right)^{\frac{1-p}{p}} \sum_j \sum_e \left[\hat{\boldsymbol{\sigma}}^{p-2}_{\mathrm{vM,e}} \rho_e^q \cdot \hat{\boldsymbol{\sigma}}_e{}^{\mathrm{T}} \mathbf{VD} \left(\mathbf{B} \Delta \mathbf{U}_e^{\{j\}} \frac{\partial R_E(\rho_e^{\{j\}})}{\partial \rho_i} - \boldsymbol{\varepsilon}^* \frac{\partial R_B(\eta_e^{\{j\}})}{\partial \rho_i} \right) \right] \tag{47}$$

$$+ A^I \left(\sum_e \hat{\sigma}^p_{\mathrm{vM},e} \right)^{\frac{1-p}{p}} \sum_e \left(\hat{\boldsymbol{\sigma}}^{p-2}_{\mathrm{vM,e}} \hat{\boldsymbol{\sigma}}_e{}^{\mathrm{T}} \mathbf{V} \boldsymbol{\sigma}_e \frac{\partial \rho_e^q}{\partial \rho_i} \right) + \sum_j \boldsymbol{\lambda}^{\{j\}} \left(\frac{\partial \mathbf{K}^{\{j\}}}{\partial \rho_i} \Delta \mathbf{U}^{\{j\}} - \frac{\partial \mathbf{F}^{\{j\}}}{\partial \rho_i} \right). \tag{48}$$

Sensitivity w.r.t design variable $\boldsymbol{\mu}$. The sensitivity analysis of the pseudo heat diffusivity variable $\boldsymbol{\mu}$ is similar to that of the density field. An adjoint analysis is also needed for the heat equation,

$$\begin{aligned} \frac{\partial g_s}{\partial \mu_i} &= \frac{\partial g_s}{\partial \mathbf{t}} \frac{\partial \mathbf{t}}{\partial \mu_i} + \boldsymbol{\lambda}_{\mathbf{T}}{}^{\top} \left(\frac{\partial \mathbf{b}}{\partial \mu_i} - \frac{\partial \mathbf{K}_{\mathrm{T}}}{\partial \mu_i} \mathbf{T} - \mathbf{K}_{\mathrm{T}} \frac{\partial \mathbf{T}}{\partial \mu_i} \right), \\ &= \left(\frac{\partial g_s}{\partial \mathbf{t}} + \boldsymbol{\lambda}_{\mathbf{T}}{}^{\top} \mathbf{K}_{\mathrm{T}} \right) \frac{\partial \mathbf{T}}{\partial \mu_i} - \boldsymbol{\lambda}_{\mathbf{T}}{}^{\top} \frac{\partial \mathbf{K}_{\mathrm{T}}}{\partial \mu_i} \mathbf{T}. \end{aligned} \tag{49}$$

The Lagrangian multiplier $\boldsymbol{\lambda}_{\mathbf{T}}$ is the same as that in Eq. (35).

Lagrangian multiplier λ. In order to solve for the Lagrangian multiplier $\boldsymbol{\lambda}_{\mathbf{T}}$ in Eqs. (35) and (49). The derivative of the residual stress constraint with respect to the time field is needed. By substituting g_s using Eq. (24), we get

$$\frac{\partial g_s}{\partial t_i} = A^I \left(\sum_e \hat{\sigma}^p_{\mathrm{vM},e} \right)^{\frac{1-p}{p}} \sum_e \left[\hat{\sigma}^{p-2}_{\mathrm{vM},e} \cdot \hat{\boldsymbol{\sigma}}_e^{\mathrm{T}} \mathbf{V} \frac{\partial \boldsymbol{\sigma}_e}{\partial t_i} \rho_e{}^q \right]. \tag{50}$$

$\frac{\partial \boldsymbol{\sigma}_e}{\partial t_i}$ is obtained according to Eqs. (7) and (12),

$$\frac{\partial \boldsymbol{\sigma}_e}{\partial t_i} = \sum_j \left(\mathbf{DB} \frac{\partial \Delta \mathbf{U}_e^{\{j\}}}{\partial t_i} R_E(\rho_e^{\{j\}}) + \mathbf{DB} \Delta \mathbf{U}_e^{\{j\}} \frac{\partial R_E(\boldsymbol{\rho}^{\{j\}})}{\partial t_i} - \mathbf{D} \boldsymbol{\varepsilon}^* \frac{\partial R_B(\eta_e^{\{j\}})}{\partial t_i} \right). \tag{51}$$

The sensitivity of the time field can also be rewritten in an augmented form:

$$\begin{aligned} \frac{\partial g_s}{\partial t_i} =& A^I \left(\sum_e \hat{\sigma}^p_{\mathrm{vM},e} \right)^{\frac{1-p}{p}} \sum_j \sum_e \left[\hat{\boldsymbol{\sigma}}^{p-2}_{\mathrm{vM,e}} \rho_e^q \cdot \hat{\boldsymbol{\sigma}}_e{}^{\mathrm{T}} \mathbf{VD} \left(\mathbf{B} \frac{\partial \Delta \mathbf{U}_e^{\{j\}}}{\partial t_i} R_E(\rho_e^{\{j\}}) + \mathbf{B} \Delta \mathbf{U}_e^{\{j\}} \frac{\partial R_E(\rho_e^{\{j\}})}{\partial t_i} - \boldsymbol{\varepsilon}^* \frac{\partial R_B(\eta_e^{\{j\}})}{\partial t_i} \right) \right] \\ &+ \sum_j \boldsymbol{\lambda}^{\{j\}} \left(\frac{\partial \mathbf{K}^{\{j\}}}{\partial t_i} \Delta \mathbf{U}^{\{j\}} + \mathbf{K}^{\{j\}} \frac{\partial \Delta \mathbf{U}^{\{j\}}}{\partial t_i} - \frac{\partial \mathbf{F}^{\{j\}}}{\partial t_i} \right). \end{aligned} \tag{52}$$

Therefore, by using the same Lagrangian multipliers as in Eq. (46), the above equation is simplified,

$$\begin{aligned} \frac{\partial g_s}{\partial t_i} =& A^I \left(\sum_e \hat{\sigma}^p_{\mathrm{vM},e} \right)^{\frac{1-p}{p}} \sum_j \sum_e \left[\hat{\boldsymbol{\sigma}}^{p-2}_{\mathrm{VM,e}} \rho_e^q \cdot \hat{\boldsymbol{\sigma}}_e{}^{\mathrm{T}} \mathbf{VD} \left(\mathbf{B} \Delta \mathbf{U}_e^{\{j\}} \frac{\partial R_E(\rho_e^{\{j\}})}{\partial t_i} - \boldsymbol{\varepsilon}^* \frac{\partial R_B(\eta_e^{\{j\}})}{\partial t_i} \right) \right] \\ &+ \sum_j \boldsymbol{\lambda}^{\{j\}} \left(\frac{\partial \mathbf{K}^{\{j\}}}{\partial t_i} \Delta \mathbf{U}^{\{j\}} - \frac{\partial \mathbf{F}^{\{j\}}}{\partial t_i} \right). \end{aligned} \tag{53}$$

Appendix B. Sensitivity analysis of the objective function

The objective function consists of two parts: the thermally induced distortion c_{thermal}, and variations in the layer geometry f_{geo}. The sensitivity analysis of the first part can be found in Wang et al. [41]. We here focus on the second part. Similar to the stress constraint, f_{geo} is also related to optimization variables $\boldsymbol{\phi}$ and $\boldsymbol{\mu}$ via the density field $\boldsymbol{\rho} = \bar{\tilde{\boldsymbol{\phi}}}$, and the time field $\boldsymbol{t}$.

Sensitivity w.r.t density $\boldsymbol{\rho}$. The sensitivity of f_{geo} in relation to density is

$$\begin{aligned} \frac{\mathrm{d} f_{\mathrm{geo}}}{\mathrm{d} \rho_i} &= \frac{\partial f_{\mathrm{geo}}}{\partial \rho_i} + \frac{\partial f_{\mathrm{geo}}}{\partial \mathbf{t}} \frac{\partial \mathbf{t}}{\partial \rho_i} + \boldsymbol{\lambda}^{\top} \left(\frac{\partial \mathbf{b}}{\partial \rho_i} - \frac{\partial \mathbf{K}_{\mathrm{T}}}{\partial \rho_i} \mathbf{T} - \mathbf{K}_{\mathrm{T}} \frac{\partial \mathbf{T}}{\partial \rho_i} \right), \\ &= \frac{\partial f_{\mathrm{geo}}}{\partial \rho_i} - \left(\frac{\partial f_{\mathrm{geo}}}{\partial \mathbf{t}} + \boldsymbol{\lambda}^{\top} \mathbf{K}_{\mathrm{T}} \right) \frac{\partial \mathbf{T}}{\partial \rho_i} - \boldsymbol{\lambda}^{\top} \frac{\partial \mathbf{K}_{\mathrm{T}}}{\partial \rho_i} \mathbf{T}. \end{aligned} \tag{54}$$

The calculation of the sensitivity of the objective function f_{geo} is also divided into two parts. The first part f_{geo} is explicitly related to the density field by treating the time field $\mathbf{t}$ as constant, while the second part f_{geo} is related to the density field through the time field. The mathematical formulations of f_{geo} and f_{geo} are the same as f_{geo}. With the formulation of f_{geo} in Eq. (27), the first part of the above equation is calculated as

$$\frac{\partial f_{\mathrm{geo}}}{\partial \rho_i} = \sum_{j=1}^{N} \frac{\partial \sum_e \eta_e^{\{j\}^\kappa} \left(|\nabla t_e| - \overline{|\nabla t|}^{\{j\}} \right)^2}{\partial \rho_i},$$

$$= \sum_{j=1}^{N} \sum_{e} [\frac{\partial \eta_e^{\{j\}^\kappa}}{\partial \rho_i} \left(|\nabla t_e| - \overline{|\nabla t|}^{\{j\}} \right)^2 + 2\eta_e^{\{j\}^\kappa} \left(|\nabla t_e| - \overline{|\nabla t|}^{\{j\}} \right) \frac{\partial \overline{|\nabla t|}^{\{j\}}}{\partial \rho_i}]. \tag{55}$$

The derivative of the gradient average $\overline{|\nabla t|}^{\{j\}}$ with respect to the density ρ_i is derived from Eq. (28):

$$\frac{\partial \overline{|\nabla t|}^{\{j\}}}{\partial \rho_i} = \frac{\frac{\partial \sum_e \eta_e^{\{j\}^\kappa} |\nabla t_e|}{\partial \rho_i} \left(\sum_e \eta_e^{\{j\}^\kappa} \right) - \left(\sum_e \eta_e^{\{j\}^\kappa} |\nabla t_e| \right) \frac{\partial \sum_e \eta_e^{\{j\}^\kappa}}{\partial \rho_i}}{\sum_e \eta_e^{\{j\}^{\kappa 2}}}. \tag{56}$$

Sensitivity w.r.t design variable $\boldsymbol{\mu}$. The sensitivity of f_{geo} in relation to the filtered thermal diffusivity $\boldsymbol{\mu}$ is calculated by using the adjoint analysis as well:

$$\begin{aligned} \frac{\partial f_{\text{geo}}}{\partial \mu_i} &= \frac{\partial f_{\text{geo}}}{\partial \mathbf{t}} \frac{\partial \mathbf{t}}{\partial \mu_i} + \boldsymbol{\lambda}^\top \left(\frac{\partial \mathbf{b}}{\partial \mu_i} - \frac{\partial \mathbf{K}_\text{T}}{\partial \mu_i} \mathbf{T} - \mathbf{K}_\text{T} \frac{\partial \mathbf{T}}{\partial \mu_i} \right), \\ &= - \left(\frac{\partial f_{\text{geo}}}{\partial \mathbf{t}} + \boldsymbol{\lambda}^\top \mathbf{K}_\text{T} \right) \frac{\partial \mathbf{T}}{\partial \mu_i} - \boldsymbol{\lambda}^\top \frac{\partial \mathbf{K}_\text{T}}{\partial \mu_i} \mathbf{T}. \end{aligned} \tag{57}$$

Lagrangian multiplier λ. To solve for the Lagrange multiplier $\boldsymbol{\lambda}$, the derivative of f_{geo} with respect to the nodal time field is needed,

$$\begin{aligned} \frac{\partial f_{\text{geo}}}{\partial \mathbf{t}} &= \sum_{j=1}^{N} \frac{\partial \sum_e \eta_e^{\{j\}^\kappa} \left(|\nabla t_e| - \overline{|\nabla t|}^{\{j\}} \right)^2}{\partial \mathbf{t}}, \\ &= \sum_{j=1}^{N} \sum_{e} [\frac{\partial \eta_e^{\{j\}^\kappa}}{\partial \mathbf{t}} \left(|\nabla t_e| - \overline{|\nabla t|}^{\{j\}} \right)^2 + 2\eta_e^{\{j\}^\kappa} (|\nabla t_e| - \overline{|\nabla t|}^{\{j\}}) \left(\frac{\partial |\nabla t_e|}{\partial \mathbf{t}} - \frac{\partial \overline{|\nabla t|}^{\{j\}}}{\partial \mathbf{t}} \right)]. \end{aligned} \tag{58}$$

Here the derivative of the gradient average $\overline{|\nabla t|}^{\{j\}}$ with respect to the nodal time field is given by

$$\frac{\partial \overline{|\nabla t|}^{\{j\}}}{\partial \mathbf{t}} = \frac{\frac{\partial \sum_e \eta_e^{\{j\}^\kappa} |\nabla t_e|}{\partial \mathbf{t}} \left(\sum_e \eta_e^{\{j\}^\kappa} \right) - \left(\sum_e \eta_e^{\{j\}^\kappa} |\nabla t_e| \right) \frac{\partial \sum_e \eta_e^{\{j\}^\kappa}}{\partial \mathbf{t}}}{\sum_e \eta_e^{\{j\}^{\kappa 2}}}. \tag{59}$$

Data availability

Data will be made available on request.

References

[1] C. Dai, C.C.L. Wang, C. Wu, S. Lefebvre, G. Fang, Y.-J. Liu, Support-free volume printing by multi-axis motion, ACM Trans. Graph. 37 (4) (2018) 134:1–134:14, http://dx.doi.org/10.1145/3197517.3201342.

[2] K. Zhang, W. Zhang, X. Ding, Multi-axis additive manufacturing process for continuous fibre reinforced composite parts, Procedia CIRP 85 (2019) 114–120, http://dx.doi.org/10.1016/j.procir.2019.09.022.

[3] D. Ding, Z. Pan, D. Cuiuri, H. Li, Wire-feed additive manufacturing of metal components: technologies, developments and future interests, Int. J. Adv. Manuf. Technol. 81 (1–4) (2015) 465–481, http://dx.doi.org/10.1007/s00170-015-7077-3.

[4] S.W. Williams, F. Martina, A.C. Addison, J. Ding, G. Pardal, P. Colegrove, Wire+ arc additive manufacturing, Mater. Sci. Technol. 32 (7) (2016) 641–647, http://dx.doi.org/10.1179/1743284715Y.0000000073.

[5] H. Lockett, J. Ding, S. Williams, F. Martina, Design for wire+ arc additive manufacture: design rules and build orientation selection, J. Eng. Des. 28 (7–9) (2017) 568–598, http://dx.doi.org/10.1080/09544828.2017.1365826.

[6] S.C.A. Costello, C.R. Cunningham, F. Xu, A. Shokrani, V. Dhokia, S.T. Newman, The state-of-the-art of wire arc directed energy deposition (WA-DED) as an additive manufacturing process for large metallic component manufacture, Int. J. Comput. Integr. Manuf. 36 (3) (2023) 469–510, http://dx.doi.org/10.1080/0951192x.2022.2162597.

[7] A.P. Nagalingam, M. Shamir, E.B. Tureyen, A.R.C. Sharman, O. Poyraz, E. Yasa, J. Hughes, Recent progress in wire-arc and wire-laser directed energy deposition (DED) of titanium and aluminium alloys, Int. J. Adv. Manuf. Technol. (2025) http://dx.doi.org/10.1007/s00170-024-14967-w.

[8] B. Wu, Z. Pan, D. Ding, D. Cuiuri, H. Li, J. Xu, J. Norrish, A review of the wire arc additive manufacturing of metals: properties, defects and quality improvement, J. Manuf. Process. 35 (2018) 127–139, http://dx.doi.org/10.1016/j.jmapro.2018.08.001.

[9] Q. Wu, T. Mukherjee, A. De, T. DebRoy, Residual stresses in wire-arc additive manufacturing – hierarchy of influential variables, Addit. Manuf. 35 (2020) 101355, http://dx.doi.org/10.1016/j.addma.2020.101355.

[10] S.-g. Chen, H.-j. Gao, Y.-d. Zhang, Q. Wu, Z.-h. Gao, X. Zhou, Review on residual stresses in metal additive manufacturing: formation mechanisms, parameter dependencies, prediction and control approaches, J. Mater. Res. Technol. 17 (2022) 2950–2974, http://dx.doi.org/10.1016/j.jmrt.2022.02.054.

[11] S. Chen, M. Xu, T. Yuan, X. Jiang, H. Zhang, X. Zheng, Thermal–microstructural analysis of the mechanism of liquation cracks in wire-arc additive manufacturing of Al–Zn–Mg–Cu alloy, J. Mater. Res. Technol. 16 (2022) 1260–1271, http://dx.doi.org/10.1016/j.jmrt.2021.12.016.

[12] T.A. Rodrigues, V. Duarte, R. Miranda, T.G. Santos, J. Oliveira, Current status and perspectives on wire and arc additive manufacturing (WAAM), Materials 12 (7) (2019) 1121, http://dx.doi.org/10.3390/ma12071121.

[13] D. Jafari, T.H.J. Vaneker, I. Gibson, Wire and arc additive manufacturing: Opportunities and challenges to control the quality and accuracy of manufactured parts, Mater. Des. (2021) 109471, http://dx.doi.org/10.1016/j.matdes.2021.109471.

[14] H. Shen, J. Lin, Z. Zhou, B. Liu, Effect of induction heat treatment on residual stress distribution of components fabricated by wire arc additive manufacturing, J. Manuf. Process. 75 (2022) 331–345, http://dx.doi.org/10.1016/j.jmapro.2022.01.018.

[15] J.W. Elmer, K. Fisher, G. Gibbs, J. Sengthay, D. Urabe, Post-build thermomechanical processing of wire arc additively manufactured stainless steel for improved mechanical properties and reduction of crystallographic texture, Addit. Manuf. 50 (2022) 102573, http://dx.doi.org/10.1016/j.addma.2021.102573.

[16] J.R. Hönnige, P.A. Colegrove, S. Ganguly, E. Eimer, S. Kabra, S. Williams, Control of residual stress and distortion in aluminium wire + arc additive manufacture with rolling, Addit. Manuf. 22 (2018) 775–783, http://dx.doi.org/10.1016/j.addma.2018.06.015.
[17] V. Gornyakov, J. Ding, Y. Sun, S. Williams, Understanding and designing post-build rolling for mitigation of residual stress and distortion in wire arc additively manufactured components, Mater. Des. 213 (2022) 110335, http://dx.doi.org/10.1016/j.matdes.2021.110335.
[18] J. Mehnen, J. Ding, H. Lockett, P. Kazanas, Design study for wire and arc additive manufacture, Int. J. Prod. Dev. 19 (1/2/3) (2014) 2, http://dx.doi.org/10.1504/ijpd.2014.060028.
[19] J. Norrish, J. Polden, I. Richardson, A review of wire arc additive manufacturing: development, principles, process physics, implementation and current status, J. Phys. D: Appl. Phys. 54 (47) (2021) 473001, http://dx.doi.org/10.1088/1361-6463/ac1e4a.
[20] G. Allaire, L. Jakabčin, Taking into account thermal residual stresses in topology optimization of structures built by additive manufacturing, Math. Models Methods Appl. Sci. 28 (12) (2018) 2313–2366, http://dx.doi.org/10.1142/s0218202518500501.
[21] G. Misiun, E. van de Ven, M. Langelaar, H. Geijselaers, F. van Keulen, T. van den Boogaard, C. Ayas, Topology optimization for additive manufacturing with distortion constraints, Comput. Methods Appl. Mech. Engrg. 386 (2021) 114095, http://dx.doi.org/10.1016/j.cma.2021.114095.
[22] S. Xu, J. Liu, Y. Ma, Residual stress constrained self-support topology optimization for metal additive manufacturing, Comput. Methods Appl. Mech. Engrg. 389 (2022) 114380, http://dx.doi.org/10.1016/j.cma.2021.114380.
[23] L. Cheng, X. Liang, J. Bai, Q. Chen, J. Lemon, A. To, On utilizing topology optimization to design support structure to prevent residual stress induced build failure in laser powder bed metal additive manufacturing, Addit. Manuf. 27 (2019) 290–304, http://dx.doi.org/10.1016/j.addma.2019.03.001.
[24] Z.-D. Zhang, O. Ibhadode, U. Ali, C.F. Dibia, P. Rahnama, A. Bonakdar, E. Toyserkani, Topology optimization parallel-computing framework based on the inherent strain method for support structure design in laser powder-bed fusion additive manufacturing, Int. J. Mech. Mater. Des. 16 (4) (2020) 897–923, http://dx.doi.org/10.1007/s10999-020-09494-x.
[25] L. Cheng, A. To, Part-scale build orientation optimization for minimizing residual stress and support volume for metal additive manufacturing: Theory and experimental validation, Computer- Aided Des. 113 (2019) 1–23, http://dx.doi.org/10.1016/j.cad.2019.03.004.
[26] M. Bruggi, V. Laghi, T. Trombetti, Simultaneous design of the topology and the build orientation of wire-and-arc additively manufactured structural elements, Comput. Struct. 242 (2021) 106370, http://dx.doi.org/10.1016/j.compstruc.2020.106370.
[27] M. Bruggi, V. Laghi, T. Trombetti, Optimal design of wire-and-arc additively manufactured I-Beams for prescribed deflection, Comput. Assist. Methods Eng. Sci. (2022) http://dx.doi.org/10.24423/cames.469.
[28] V. Laghi, M. Palermo, M. Bruggi, G. Gasparini, T. Trombetti, Blended structural optimization for wire-and-arc additively manufactured beams, Prog. Addit. Manuf. 8 (3) (2023) 381–392, http://dx.doi.org/10.1007/s40964-022-00335-1.
[29] K. Wu, W. Wang, F. van Keulen, J. Wu, Space–time topology optimization for anisotropic materials in wire and arc additive manufacturing, Int. J. Mech. Sci. 284 (2024) 109712, http://dx.doi.org/10.1016/j.ijmecsci.2024.109712.
[30] D. Ding, Z. Pan, D. Cuiuri, H. Li, A tool-path generation strategy for wire and arc additive manufacturing, Int. J. Adv. Manuf. Technol. 73 (1–4) (2014) 173–183, http://dx.doi.org/10.1007/s00170-014-5808-5.
[31] D. Ding, Z. Pan, D. Cuiuri, H. Li, A practical path planning methodology for wire and arc additive manufacturing of thin-walled structures, Robot. Comput.-Integr. Manuf. 34 (2015) 8–19, http://dx.doi.org/10.1016/j.rcim.2015.01.003.
[32] D. Ding, Z. Pan, D. Cuiuri, H. Li, S. van Duin, N. Larkin, Bead modelling and implementation of adaptive MAT path in wire and arc additive manufacturing, Robot. Comput.-Integr. Manuf. 39 (2016) 32–42, http://dx.doi.org/10.1016/j.rcim.2015.12.004.
[33] T. Zhang, G. Fang, Y. Huang, N. Dutta, S. Lefebvre, Z.M. Kilic, C.C. Wang, S3-slicer: A general slicing framework for multi-axis 3D printing, ACM Trans. Graph. 41 (6) (2022) 1–15, http://dx.doi.org/10.1145/3550454.3555516.
[34] V. Beik, H. Marzbani, R. Jazar, Welding sequence optimisation in the automotive industry: A review, Proc. Inst. Mech. Eng. Part C: J. Mech. Eng. Sci. 233 (17) (2019) 5945–5952, http://dx.doi.org/10.1177/0954406219859909.
[35] C. Wu, C. Wang, J.-W. Kim, Welding sequence optimization to reduce welding distortion based on coupled artificial neural network and swarm intelligence algorithm, Eng. Appl. Artif. Intell. 114 (2022) 105142, http://dx.doi.org/10.1016/j.engappai.2022.105142.
[36] W. Wang, F. van Keulen, J. Wu, Fabrication sequence optimization for minimizing distortion in multi-axis additive manufacturing, Comput. Methods Appl. Mech. Engrg. 406 (2023) 115899, http://dx.doi.org/10.1016/j.cma.2023.115899.
[37] Q. Chen, J. Liu, X. Liang, A.C. To, A level-set based continuous scanning path optimization method for reducing residual stress and deformation in metal additive manufacturing, Comput. Methods Appl. Mech. Engrg. 360 (2020) 112719, http://dx.doi.org/10.1016/j.cma.2019.112719.
[38] M. Boissier, G. Allaire, C. Tournier, Additive manufacturing scanning paths optimization using shape optimization tools, Struct. Multidiscip. Optim. 61 (6) (2020) 2437–2466, http://dx.doi.org/10.1007/s00158-020-02614-3.
[39] M. Boissier, G. Allaire, C. Tournier, Concurrent shape optimization of the part and scanning path for powder bed fusion additive manufacturing, SIAM J. Control Optim. 61 (2) (2023) 697–722, http://dx.doi.org/10.1137/21M1461976.
[40] W. Wang, D. Munro, C.C. Wang, F. van Keulen, J. Wu, Space-time topology optimization for additive manufacturing, Struct. Multidiscip. Optim. 61 (1) (2020) 1–18, http://dx.doi.org/10.1007/s00158-019-02420-6.
[41] W. Wang, K. Wu, F. van Keulen, J. Wu, Regularization in space–time topology optimization for additive manufacturing, Comput. Methods Appl. Mech. Engrg. 431 (2024) 117202, http://dx.doi.org/10.1016/j.cma.2024.117202.
[42] Y. Ueda, H. Murakawa, K. Nakacho, N.X. Ma, Establishment of computational welding mechanics, Weld. Surf. Rev. 8 (1) (1997) 265–299, http://dx.doi.org/10.18910/3926.
[43] V. Ploshikhin, A. Prihodovsky, A. Ilin, C. Heimerdinger, Advanced numerical method for fast prediction of welding distortions of large aircraft structures, Int. J. Microstruct. Mater. Prop. 5 (4–5) (2010) 423–435, http://dx.doi.org/10.1504/IJMMP.2010.037619.
[44] X. Liang, Q. Chen, L. Cheng, D. Hayduke, A.C. To, Modified inherent strain method for efficient prediction of residual deformation in direct metal laser sintered components, Comput. Mech. 64 (6) (2019) 1719–1733, http://dx.doi.org/10.1007/s00466-019-01748-6.
[45] D. Munro, C. Ayas, M. Langelaar, F. van Keulen, On process-step parallel computability and linear superposition of mechanical responses in additive manufacturing process simulation, Addit. Manuf. (2019) http://dx.doi.org/10.1016/j.addma.2019.06.023.
[46] I. Setien, M. Chiumenti, S. van der Veen, M. San Sebastian, F. Garciandía, A. Echeverría, Empirical methodology to determine inherent strains in additive manufacturing, Comput. Math. Appl. 78 (7) (2019) 2282–2295, http://dx.doi.org/10.1016/j.camwa.2018.05.015.
[47] J. Ding, P. Colegrove, J. Mehnen, S. Ganguly, P.M. Sequeira Almeida, F. Wang, S. Williams, Thermo-mechanical analysis of wire and arc additive layer manufacturing process on large multi-layer parts, Comput. Mater. Sci. (2011) http://dx.doi.org/10.1016/j.commatsci.2011.06.023.
[48] A. Lundbäck, L.-E. Lindgren, Modelling of metal deposition, Finite Elem. Anal. Des. 47 (10) (2011) 1169–1177, http://dx.doi.org/10.1016/j.finel.2011.05.005.
[49] J. Ding, P. Colegrove, J. Mehnen, S. Williams, F. Wang, P.S. Almeida, A computationally efficient finite element model of wire and arc additive manufacture, Int. J. Adv. Manuf. Technol. 70 (1–4) (2013) 227–236, http://dx.doi.org/10.1007/s00170-013-5261-x.
[50] T. Mukherjee, W. Zhang, T. DebRoy, An improved prediction of residual stresses and distortion in additive manufacturing, Comput. Mater. Sci. 126 (2017) 360–372, http://dx.doi.org/10.1016/j.commatsci.2016.10.003.
[51] P. Duysinx, O. Sigmund, New developments in handling stress constraints in optimal material distribution, in: 7th AIAA/USAF/NASA/ISSMO Symposium on Multidisciplinary Analysis and Optimization, 1998, http://dx.doi.org/10.2514/6.1998-4906.
[52] R.J. Yang, C.J. Chen, Stress-based topology optimization, Struct. Optim. 12 (2–3) (1996) 98–105, http://dx.doi.org/10.1007/bf01196941.

[53] G.A. Da Silva, N. Aage, A.T. Beck, O. Sigmund, Three-dimensional manufacturing tolerant topology optimization with hundreds of millions of local stress constraints, Internat. J. Numer. Methods Engrg. 122 (2) (2021) 548–578, http://dx.doi.org/10.1002/nme.6548.
[54] X. Zhai, F. Chen, J. Wu, Alternating optimization of design and stress for stress-constrained topology optimization, Struct. Multidiscip. Optim. (2021) http://dx.doi.org/10.1007/s00158-021-02985-1.
[55] G.D. Cheng, X. Guo, ϵ-Relaxed approach in structural topology optimization, Struct. Optim. 13 (4) (1997) 258–266, http://dx.doi.org/10.1007/bf01197454.
[56] M. Bruggi, On an alternative approach to stress constraints relaxation in topology optimization, Struct. Multidiscip. Optim. 36 (2) (2008) 125–141, http://dx.doi.org/10.1007/s00158-007-0203-6.
[57] C. Le, J. Norato, T. Bruns, C. Ha, D. Tortorelli, Stress-based topology optimization for continua, Struct. Multidiscip. Optim. 41 (4) (2010) 605–620, http://dx.doi.org/10.1007/s00158-009-0440-y.
[58] A. Verbart, M. Langelaar, F.v. Keulen, A unified aggregation and relaxation approach for stress-constrained topology optimization, Struct. Multidiscip. Optim. 55 (2) (2016) 663–679, http://dx.doi.org/10.1007/s00158-016-1524-0.
[59] M.P. Bendsøe, O. Sigmund, Material interpolation schemes in topology optimization, Arch. Appl. Mech. (Ing. Archiv) 69 (9–10) (1999) 635–654, http://dx.doi.org/10.1007/s004190050248.
[60] F. Wang, B.S. Lazarov, O. Sigmund, On projection methods, convergence and robust formulations in topology optimization, Struct. Multidiscip. Optim. 43 (6) (2011) 767–784, http://dx.doi.org/10.1007/s00158-010-0602-y.
[61] K. Svanberg, The method of moving asymptotes—a new method for structural optimization, Internat. J. Numer. Methods Engrg. 24 (2) (1987) 359–373, http://dx.doi.org/10.1002/nme.1620240207.